https://doi.org/10.5194/egusphere-2026-6281
Preprint. Discussion started: 4 November 2026
© Author(s) 2026. CC BY 4.0 License.

Design and performance of a FLOw TUbe System, FLOTUS, for the CERN CLOUD chamber

Eva Sommer[1, 2], Mattia Busato[1], Pedro Rato[1, 3], Hannah Klebach[3], Nirvan Bhattacharyya[3], Yuanlong Huang[4, 5], Didier Lombard[1], Bernhard Mentler[6], Zhensen Zheng[6, 7], Theodoros Aivaliotis[1], João Almeida[1, 8], Louis-Philippe De Menezes[1], Ilia Krasin[1], Robert Kristic[1], Giulio Malaguti[1], Pierre Minginette[1], Sylvain Ravat[1], Emiliano Urrutia[1], Stefan Weber[1], Lubna Dada[9], Jenna De Vivo[10, 11, 12], Milin Kaniyodical Sebastian[13], Paap Koemets[14], Felix Kunkler[15], Wiebke Scholz[6], Prashant Tripathi[16,17], Jens Voigtländer[18], Theodoros Christoudias[19], Joachim Curtius[3], Neil Donahue[10, 11, 20], Imad El Haddad[9], Roberto Guida[1], Armin Hansel[6], Hartwig Harder[15], Xu-Cheng He[21], Liine Heikkinen[16,17], Heikki Junninen[14], Markku Kulmala[21, 22], Katrianne Lehtipalo[21, 22, 23], Ottmar Möhler[13], Mira Pöhlker[18], Rainer Volkamer[24, 25], Paul Martin Winkler[2], Richard C. Flagan[4], Antti Onnela[1], Serge Mathot[1], and Jasper Kirkby[1, 3]

[1]CERN, Esplanade des Particules 1, 1217 Meyrin, Switzerland
[2]University of Vienna, Faculty of Physics, Boltzmanngasse 5, 1090 Vienna, Austria
[3]Institute for Atmospheric and Environmental Science, Goethe University Frankfurt, Altenhöferallee 1, 60438 Frankfurt am Main, Germany
[4]California Institute of Technology, Pasadena, 91125 California, United States
[5]Eastern Institute of Technology, Ningbo, Zhejiang Province, China
[6]Institute for Ion and Applied Physics, University of Innsbruck, Technikerstraße 25, 6020 Innsbruck, Austria
[7]IONICON Analytik GmbH, 6020 Innsbruck, Austria
[8]LIP - Laboratory for Instrumentation and Experimental Particle Physics, Av. Prof. Gama Pinto, n.2, 1649-003 Lisboa, Portugal
[9]PSI - Paul Scherrer Institute, Forschungsstrasse 111, 5232 Villigen, Switzerland
[10]Center for Atmospheric Particle Studies, CMU, 5000 Forbes Ave Pittsburgh PA USA 15213
[11]Department of Chemistry, CMU, 5000 Forbes Ave Pittsburgh PA USA 15213
[12]University of Manchester School of Earth, Atmospheric and Environmental Sciences Simon Building Oxford Road Manchester M13 9PL, United Kingdom
[13]Karlsruhe Institute of Technology Institute of Meteorology and Climate Research, Karlsruhe, Germany Postfach 3640, 76133 Karlsruhe, Germany
[14]Laboratory of Atmospheric and Environmental Sciences, Institute of Physics, University of Tartu, Estonia
[15]Atmospheric Chemistry Department - Max Planck Institute for Chemistry, Hahn-Meitner-Weg 1, 55128 Mainz, Germany
[16]Department of Environmental Science, Stockholm University, Sweden
[17]Bolin Centre for Climate Research, Stockholm University, Sweden
[18]Leibniz Institute for Tropospheric Research e.V. (TROPOS), Permoserstraße 15, 04318 Leipzig, Germany
[19]The Cyprus Institute, Climate and Atmosphere Research Center, 2121 Nicosia, Cyprus
[20]Department of Chemical Engineering, CMU, 5000 Forbes Ave Pittsburgh PA USA 15213
[21]Institute for Atmospheric and Earth System Research/Physics, University of Helsinki, Helsinki, Finland
[22]Helsinki Institute of Physics, University of Helsinki, Helsinki, Finland
[23]Finnish Meteorological Institute, Helsinki, Finland
[24]Department of Chemistry, University of Colorado Boulder, 215 UCB, Boulder, CO, USA
[25]CIRES, Cooperative Institute for Research in Environmental Sciences, University of Colorado Boulder, 216 UCB, Boulder, CO, USA

https://doi.org/10.5194/egusphere-2026-6281
Preprint. Discussion started: 4 November 2026
© Author(s) 2026. CC BY 4.0 License.



Correspondence:
Eva Sommer (eva.sommer@cern.ch)
Jasper Kirkby (jasper.kirkby@cern.ch)

Abstract. The primary functions of the FLOw TUbe System (FLOTUS) are to provide the CERN CLOUD chamber with a source of a) pre-aged organic vapours and particles, and b) cloud condensation nuclei (CCN) of any chosen chemical composition and diameter. The quartz flow tube has 20 cm internal diameter and 60 L volume, and it operates between $-45\,^{\circ}\mathrm{C}$ and $+100\,^{\circ}\mathrm{C}$, limited by the currently-installed thermoregulator. All the experimental conditions in FLOTUS are controlled independently of CLOUD: ultrapure air flow, trace-gases, ozone, UV illumination, humidity and temperature. The vapours and particles produced in FLOTUS can be transferred either directly to analysing instruments or else injected into the CLOUD chamber for further experiments with a comprehensive suite of analysing instruments. Computational Fluid Dynamics (CFD) calculations indicate that up to 32 % transfer efficiency from FLOTUS to CLOUD can be achieved for sticky vapours of 1 nm mobility diameter, despite a long transfer pipe (3.42 m) with two 90° bends. Special attention is given in the design to minimise turbulence in the quartz flow tube: it is mounted vertically to avoid transverse convective turbulence from heating by the UV lamps, and the entrance and exit geometries are narrow-angle cones. We have analysed the residence time distributions of brief injections of toluene assuming an axially-dispersed plug-flow-reactor model. We measure Péclet numbers between 8.2 and 73 for flow rates of 15 to 45 $\mathrm{L\,min^{-1}}$, respectively, indicating that bulk transport of molecules dominates over diffusion and turbulence. Hydroxyl (OH) radicals are produced in FLOTUS by photolysis of ozone in the presence of water vapour. At 30 $\mathrm{L\,min^{-1}}$ flow rate, we measure a mean OH exposure of up to $3 \cdot 10^{11}\ \mathrm{cm^{-3}s}$, which corresponds to $3 \cdot 10^{9}\ \mathrm{cm^{-3}}$ mean OH concentration and is equivalent to several days OH exposure under ambient conditions. FLOTUS produces aerosol particles from diverse inorganic and organic precursors, with self-preserving, close to log normal size distributions characteristic of coagulation-dominated growth. Aerosol particles can be produced with geometric mean diameters between 8.0 and 136 nm and with geometric standard deviations between 1.16 and 1.43. High particle injection rates into the CLOUD chamber are achieved of up to around 20 $\mathrm{cm^{-3}s^{-1}}$. High-resolution aerosol mass spectra show that the organic aerosol composition varies with the precursor system and the OH exposure, and is in good agreement with ambient measurements of aged organic aerosol. These initial results establish FLOTUS as an important extension of the CERN CLOUD chamber for novel experiments involving aged organic vapours, cloud condensation nuclei and aerosol-cloud processing.

1 Introduction

Atmospheric aerosol particles affect the global climate either directly by interacting with radiation, or indirectly by acting as cloud condensation nuclei (CCN) which influence cloud microphysical properties. Globally, more than half of all CCN originate from new particle formation (Gordon et al., 2017). These newly formed aerosol particles must grow to larger sizes (at least 50 nm in diameter) before they can participate in cloud formation, and the chemistry controlling their formation and growth depends on precursor composition and environmental conditions (Kulmala et al., 2013). Particle size and chemical composition also determine whether particles activate into cloud droplets.

https://doi.org/10.5194/egusphere-2026-6281
Preprint. Discussion started: 4 November 2026
© Author(s) 2026. CC BY 4.0 License.

The CERN CLOUD experiment is designed to study the nucleation and growth of aerosol particles and their interactions with cloud droplets under controlled atmospheric conditions (Kirkby et al., 2011). The 26.1 m^3 CLOUD chamber provides an ultra-clean environment in which trace gases, ion concentrations, water vapour and temperature can be stably controlled over long periods. In most experiments, the particles are formed from precursor vapours injected into the chamber. They are then oxidised by ozone or hydroxyl radicals to yield low volatility vapours. Particle growth rates at atmospheric conditions are frequently below 1 $\mathrm{nm\,h^{-1}}$, so the particles may grow to diameters of only a few nm—well below CCN sizes—before they are lost to the chamber walls. (The wall loss rate in the CLOUD chamber at standard 12% mixing fans speed is $1.7 \cdot 10^{-3}/\mathrm{d_p}$ $(\mathrm{s^{-1}})$, where $\mathrm{d_p}$ (nm) is the mobility diameter of the vapour or particle in air.) Furthermore, organic vapours in the atmosphere generally experience multiple oxidation reactions with hydroxyl radicals over periods of several hours to days, with each reaction altering their oxygenation state and volatility. These ageing processes of organic vapours cannot be simulated in the CLOUD chamber alone.

To overcome these limitations, we have recently installed a FLOw TUbe System (FLOTUS) at the CLOUD chamber that generates particles and vapours which can be either directly analysed or else transferred to the chamber for extended experiments with its full suite of analysing instruments. Previous flow reactors have demonstrated their ability to generate high OH levels and aged secondary organic aerosol equivalent to several days exposure in the atmosphere (Lambe et al., 2011). FLOTUS follows the design of the Caltech Photooxidation Flow Tube (CPOT) with narrow-angle conical entrance and exit geometries, plus a small of swirl of the entering flow to minimise turbulence (Huang et al., 2017; Huang and Seinfeld, 2019). The quartz flow tube has 20 cm internal diameter and 60 L volume, and is mounted vertically to avoid turbulence from heating by the UV lamps.

All the experimental conditions of FLOTUS, such as flow rates, trace gas concentrations, UV illuminations, relative humidity and temperature, are controlled independently of CLOUD. This provides great flexibility in preparing particles and vapours for injection into the CLOUD chamber operating at different experimental conditions. As an example, CCN of any chosen chemical composition can be prepared in FLOTUS under relatively warm and humid conditions and then transferred to the CLOUD chamber operating near 100 % relative humidity at a lower temperature. This drives the CLOUD chamber into supersaturation and so the CCN activate to form persistent droplets or ice particles, allowing experiments to be performed on aerosol-cloud processing. A second example is that FLOTUS can provide a clean, independent source of hydroperoxyl (HO_2) radicals for experiments in the CLOUD chamber where oxidation proceeds via organic peroxy radicals (RO_2). Here, the trace gases injected into FLOTUS are ozone and carbon monoxide (the synthetic air already includes 100 ppbv CO contaminant). Hydroperoxyl radicals are produced by the reactions $OH + CO(+O_2) \rightarrow HO_2 + CO_2$ and $OH + O_3 \rightarrow HO_2 + O_2$. The main loss of HO_2 is with OH, so this reaction is shut off as soon as OH production ceases at the exit of FLOTUS.

In the following we will first describe the design of FLOTUS as well as our computational fluid dynamics (CFD) simulations that informed the design choices. In the second part, we will present our initial measurements of the performance of FLOTUS for gas residence time, hydroxyl radical exposure, generation of CCN and aging of organic aerosol.

https://doi.org/10.5194/egusphere-2026-6281
Preprint. Discussion started: 4 November 2026
© Author(s) 2026. CC BY 4.0 License.

2 FLOTUS design and instrumentation

2.1 Mechanical design

Figure 1a) shows a schematic of FLOTUS. The system is instrumented with Pt100 temperature sensors, photodiodes and pressure sensors, with locations as shown in Fig. 1b). The central component of FLOTUS is a 60 L flow tube made entirely of quartz (Fig. 1c), with the exception of delicate quartz-to-metal glass transition sections at the entrance and exit. The latter matches expansion coefficients to allow the welding of stainless steel bellows to the entrance and exit of the quartz tube, and operation over a wide temperature range. To maintain the ultra clean standards of the CLOUD chamber, only quartz, stainless steel and ceramics are in contact with the air flowing through FLOTUS, with the exception of the Nafion membrane used for humidification of the wet flow.

The flow tube consists of a conical inlet, a cylindrical reaction section, and a conical outlet, following the geometry of the Caltech flow reactor, CPOT (Huang et al., 2017). The cylindrical reaction section has an inner diameter of 20 cm and a length of 1.34 m. The inlet cone opens at a full angle of 10°, and the outlet cone closes at 20°. The tube is mounted vertically and the sample flow is directed from the bottom to the top for efficient transfer of the output of FLOTUS into the top of the CLOUD chamber. The UV illumination is provided by 6 independently-controlled O_3-free low pressure Hg lamps (Heraeus NNI 50/26XL), each providing 19 W optical power at 254 nm (Fig. 1c). The lamps are housed in quartz tubes through which desiccated air is passed to remove parasitic thermal power. The inner surface of the thermal housing is covered with a PTFE-based diffusive reflector to distribute the lamp output uniformly around the quartz tube.

An Air Handling Unit (AHU) recirculates temperature-controlled desiccated air through a heat exchanger and the insulated thermal housing. At the highest flow rate of 2750 $\mathrm{m^3h^{-1}}$, there is 2.5 mbar pressure difference between the outlet and inlet of the AHU (between P1 and P3 in Fig. 1b). This closed circuit controls the temperature of the reactor and removes additional heat from the UV lamps. A thermoregulator controls the temperature of the thermal fluid in the heat exchanger to maintain the circulating air temperature at a chosen setpoint that is measured by a Pt100 sensor located near the top of the FLOTUS thermal housing. The currently-installed thermoregulator allows FLOTUS operation between -45 °C. and +100 °C

2.2 Inlet and gas system

FLOTUS has a gas system that can be operated independently of CLOUD. The carrier gas is prepared from cryogenic nitrogen and oxygen at a mixing ratio of 79:21. Mass-flow controllers set the dry carrier-gas flow. A controlled fraction of the gas passes through a Nafion humidifier, which is normally held at 30 °C but can be operated between 10 °C and 50 °C. Mixing the dry and humidified streams sets the water-vapour concentration. Ozone is generated by passing a controlled flow of pure oxygen over an ozone-generating UV lamp (185 nm). The humidifier and ozone-generator systems are copies of those used for the CERN CLOUD chamber (Kirkby et al., 2011) and can be operated independently. The combined carrier-gas stream passes through a serpentine tube located inside the FLOTUS thermal housing, bringing it into thermal equilibrium before entering the reactor.

Trace gases are introduced to the humidified air stream via separate ports (Fig. 1a). The trace gases are derived from gas cylinders or temperature-controlled stainless steel evaporators. The vapours are highly diluted prior to injection into FLOTUS

https://doi.org/10.5194/egusphere-2026-6281
Preprint. Discussion started: 4 November 2026
© Author(s) 2026. CC BY 4.0 License.

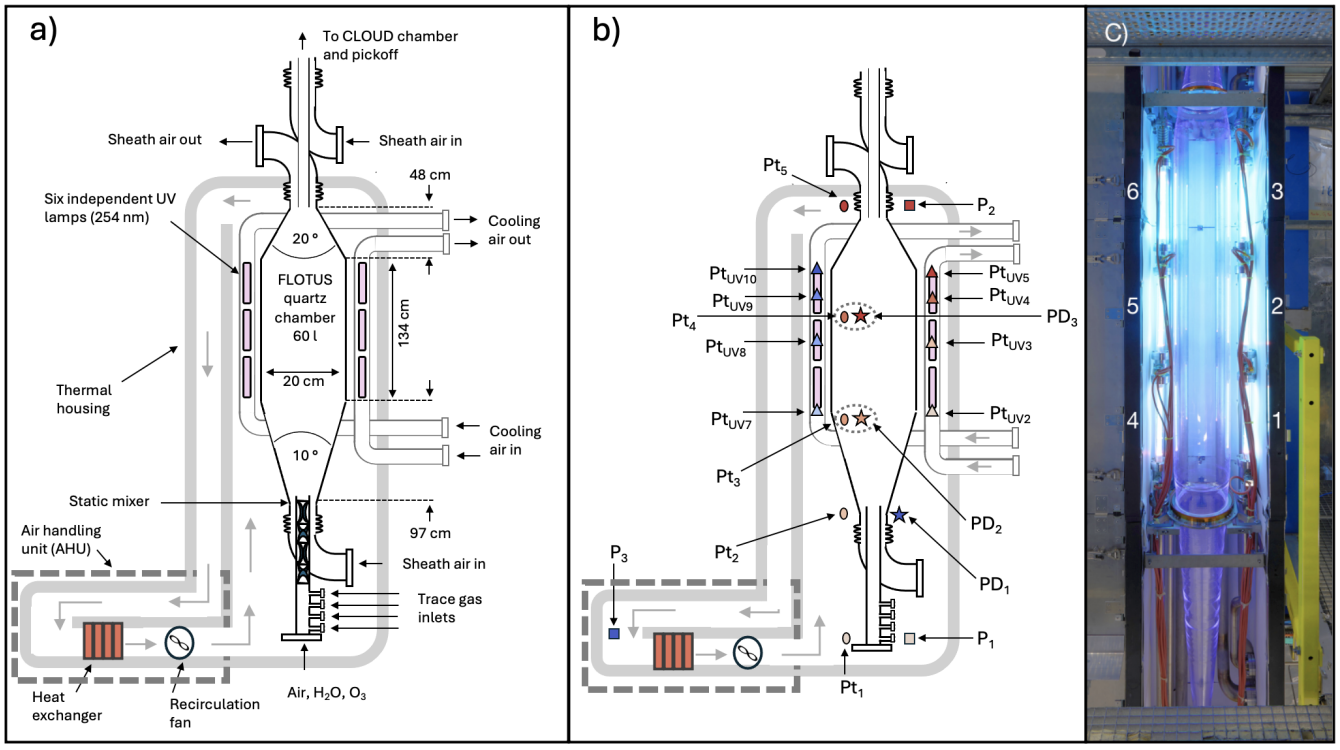


Figure 1. Schematic of FLOTUS and a photograph with the UV lamps switched on. Panel a) shows the FLOTUS components and dimensions. Panel b) shows the sensor locations and their labels: Pt100 temperature sensors (Pt_{XX}), photodiodes (PD_X) and pressure (P) sensors. The Pt100 sensors measure both the circulating air temperature (denoted by Pt_X) and also the temperature of each UV lamp (Pt_{UVX}). Three photodiodes (PD) monitor the UV intensity at the lower, middle, and upper part of the reactor, respectively. Sensors Pt_3, Pt_4, PD_2 and PD_3 are located at the back wall inside the thermal housing, behind the quartz tube. Panel c) shows a photograph of the FLOTUS quartz chamber during installation at CLOUD, without the thermal housing door and with the six UV lamps switched on (the UV lamp numbers are indicated).

https://doi.org/10.5194/egusphere-2026-6281
Preprint. Discussion started: 4 November 2026
© Author(s) 2026. CC BY 4.0 License.

using a three-MFC dilution and carrier gas scheme, similar to that used for the CLOUD chamber. Immediately downstream of the trace-gas inlets, the air flow passes through a stainless steel static mixer containing 12 helical elements (Huang et al., 2017). The static mixer ensures a completely homogeneous gas mixture before the flow enters the conical diffuser of the quartz chamber. It also introduces and azymuthal (swirl) motion to the incoming flow that reduces recirculation in the conical expansion and the risk of turbulence. The diffuser expands the flow from a 3.5 cm pipe to the 20 cm reaction section with an opening angle of 10°, while introducing minimal turbulence. An additional 1 L min^{-1} flow of ultrapure dry air (labeled sheath air in) surrounds the mixer outlet during normal operation. This sheath flow flushes the lower tube volume and minimises turbulence in the conical entrance cone.

2.3 Outlet and transfer pipe to CLOUD

As indicated in Fig. 1, the outlet cone reduces the reactor diameter from 20 to 3 cm at a cone angle of 20°. Fig. 2 shows a schematic of the FLOTUS-to-CLOUD transfer system. A 16 mm inner diameter (ID) sampling tube extracts the core flow Q_c from FLOTUS while the surrounding annular flow is removed as 'sheath air out'. Vapours that are not subject to high wall losses (O_3 and H_2O) are measured in the sheath air out. Core sampling limits the contribution of gas that has travelled close to the reactor wall. A sheath flow Q_sh can be added around the core flow before it enters the 34.8 mm ID transfer pipe to increase the transmission efficiency of aerosol particles and minimise turbulence. The transfer line reaches a Y-junction 21 cm downstream of the core inlet. The main branch continues along a 34.8 mm ID pipe for approximately 3.21 m into CLOUD, and includes two 90° bends with 50 cm radius of curvature. A gate valve is installed just before the tube enters the CLOUD thermal housing. Opening this valve starts the injection of vapours and particles from FLOTUS into CLOUD. The other branch from the Y-junction (the 'pickoff pipe') has 9.4 mm ID and extends 2.51 m to an analysing instrument such as a mass spectrometer located on a platform at the top of the CLOUD thermal housing. The pickoff flow rate (L min^{-1}) is denoted by Q_p, and the flow rate transferred to CLOUD is denoted by Q_t. Under steady conditions, and with the gate valve open, $Q_\mathrm{t} = Q_\mathrm{c} + Q_\mathrm{sh} - Q_\mathrm{p}$.

The transfer scheme shown in Fig. 2 allows for three separate modes of FLOTUS operation: 1) with the gate valve open and the pickoff closed, all the contents from FLOTUS can be directed to the CLOUD chamber, 2) with the gate valve closed and the pickoff open, we can analyse the contents of FLOTUS in parallel with ongoing experiments in the CLOUD chamber, without disturbing them, and 3) with both the gate valve and pickoff open, we can simultaneously measure the vapours and particles directly produced by FLOTUS and after they have been injected and reacted in the CLOUD chamber. A dual safety system consisting of a pressure regulation valve and a water bubbler, installed on the sheath air outflow pipe, protects the fragile quartz tube from over-pressure in an event where both pickoff and gate valve would be closed. The pressure regulation valve also ensures a stable pressure of around 8 mbar above atmospheric pressure inside FLOTUS at all times, slightly above the 5 mbar relative pressure in the CLOUD chamber, to ensure no back-flow from CLOUD along the transfer pipe.

2.4 Analysing instruments

Most of the measurements presented here were made with instruments attached to the FLOTUS pickoff (the few exceptions are explicitly stated). We monitor O_3 with a Thermo Environmental Instruments TEI 49C photometric analyser. We use chilled

https://doi.org/10.5194/egusphere-2026-6281
Preprint. Discussion started: 4 November 2026
© Author(s) 2026. CC BY 4.0 License.

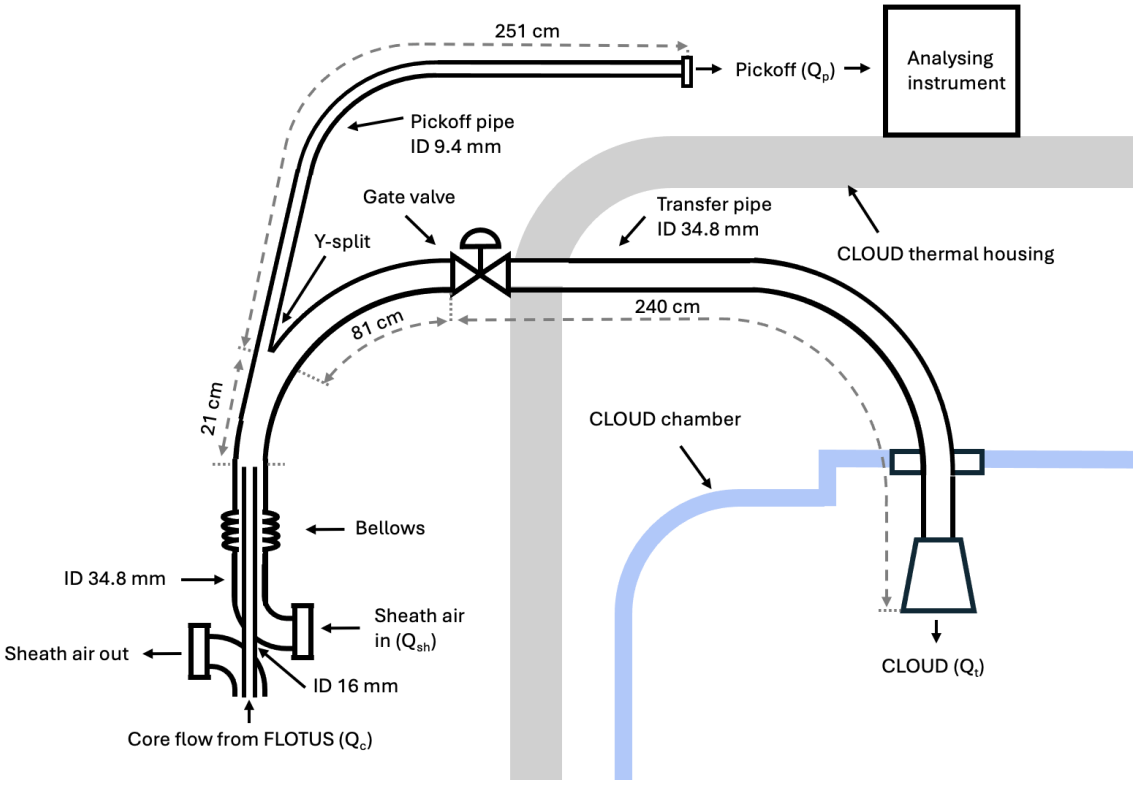


Figure 2. Schematic of the FLOTUS pickoff and transfer pipes. A 16 mm inner diameter (ID) tube takes the core flow Q_c from FLOTUS into the 34.8 mm ID transfer pipe. The sheath air out of FLOTUS is used for measurements of relative humidity and ozone, and for control of the pressure inside the quartz reactor. A sheath flow Q_{sh} can be added to the core flow to increase the downstream transmission efficiency. The transfer pipe divides at a Y-junction into the main branch towards the CLOUD chamber, with flow Q_t, and a 9.4 mm ID pickoff branch, with flow Q_p. The pickoff flow can be used to analyse the FLOTUS contents directly without injection into CLOUD. A gate valve is located on the transfer pipe to allow FLOTUS operation without any connection to the CLOUD chamber.

dew-point mirror hygrometers (DewMaster, Edgetech Instruments, and MBW 973S, Process Insights) to measure the dew point in the sheath air outflow of FLOTUS. We use a H_3O^+-PTR-MS (STOF) (Graus et al., 2011) to measure toluene during the residence-time and OH experiments. The residence-time measurements have a time resolution of 1 s. We measure particle number-size distributions with scanning mobility particle sizers (SMPSs) (Wang and Flagan, 1990). We measure non-refractory submicrometre aerosol composition with a high-resolution time-of-flight aerosol mass spectrometer (HR-ToF-AMS; Aerodyne Research, Inc.). The operating principle of the AMS and the time-of-flight implementation are described by Jayne et al. (2000) and Drewnick et al. (2005), respectively. The instrument focuses the sampled particles, vaporises the non-refractory material, ionises the vapour, and records the resulting mass spectrum (Jimenez et al., 2009). For this study, the AMS sampled from the FLOTUS pickoff through an approximately 6 m stainless-steel line. The line flow was 3 L min^{-1}, and a Nafion dryer was

https://doi.org/10.5194/egusphere-2026-6281
Preprint. Discussion started: 4 November 2026
© Author(s) 2026. CC BY 4.0 License.

installed upstream of the AMS. We calibrated the AMS with atomised, size-selected ammonium nitrate particles. The data were analysed in Igor Pro 9 (WaveMetrics, Inc.) using SQUIRREL v1.67 and PIKA v1.27.

3 Computational Fluid Dynamics (CFD) simulations

3.1 Air flow profile

We carried out CFD simulations to assess the air flow profiles inside the quartz reactor chamber. We simulated the air flow through the static mixer, inlet cone, cylindrical section and outlet cone at total flow rates of 10, 30 and 50 $\mathrm{L\,min^{-1}}$. All simulations include our standard operating mode with 1 $\mathrm{L\,min^{-1}}$ sheath air in flow included in the total flow rates reported here. The CFD simulations were performed using ANSYS Fluent 2024 R2 (ANSYS, Inc., 2024), a finite-volume-based solver. The Shear Stress Transport (SST) k-ω turbulence model (Menter, 1994) was employed to capture the turbulent flow characteristics, as it effectively balances accuracy and computational efficiency for wall-bounded flows. The computational domain was discretized into an unstructured mesh comprising approximately 700,000 cells. We applied the following boundary conditions: at the inlet, a constant mass flow rate was prescribed, while the outlet was kept at a static pressure of 1 bar. The working fluid was assumed to be air with a density of 1.225 $\mathrm{kgm^{-3}}$ and dynamic viscosity of $1.789 \cdot 10^{-5}$ $\mathrm{kgms^{-1}}$. A second-order upwind scheme (Leonard, 1979) was used for spatial discretisation of the momentum and turbulence equations, and the SIMPLE algorithm (Patankar and Spalding, 1983) was applied for pressure-velocity coupling. Convergence was considered reached when the residuals for all equations dropped below 10^{-5}, and the monitored flow variables stabilised to within 0.1% over 500 iterations.

A selection of gas velocity CFD simulations are shown in Fig. 3. Panel a) shows the verlcity magnitude throughout the flow tube at a total flow of 10 $\mathrm{L\,min^{-1}}$. Under none of the simulated input flow rates (10, 30 and 50 $\mathrm{L\,min^{-1}}$) do we find any resolved reverse-flow region. An additional simulation with an imposed 4 °C axial temperature difference between the inlet and the outlet shows no resolved change in the reported velocity pattern. For comparison, the largest temperature difference measured during steady-state operation between sensors $\mathrm{Pt_1}$ and $\mathrm{Pt_5}$, i.e. the full length of the quartz chamber (Fig. 1c), from -40 ° and $+5$ °C was around 1 °C with all six lamps illuminated.

In Figs. 3 and 4, we examine six cross-sections between $z = 32$ and 270 cm vertical distance from the mixer outlet. The static mixer produces a non-axisymmetric velocity pattern near the FLOTUS inlet, as can be seen in Figs. 3a–d) and Fig. 4a), slices 1–3). This structure weakens downstream and approaches a laminar (parabolic) flow profile earlier along the tube at lower flow rates. At slice 3, which is at the start of the cylindrical reaction section (Fig. 3a), the 10 $\mathrm{L\,min^{-1}}$ the profile is already close to parabolic, while the 30 and 50 $\mathrm{L\,min^{-1}}$ profiles still retain an imprint of the mixer. In Fig. 4b) we use slice 5) to fit the axial velocity along a central diameter with a power-law velocity profile expressed as

$$\frac{u(r)}{u_{\max}} = 1 - \left(\frac{|r|}{R}\right)^{m} \tag{1}$$

where u denotes the gas velocity, r the radial distance from the tube axis, $R = 10\,\mathrm{cm}$ is the tube radius and m describes the profile shape. The parabolic profile of fully developed laminar flow has $m = 2$, whereas a developing velocity profile has

https://doi.org/10.5194/egusphere-2026-6281
Preprint. Discussion started: 4 November 2026
© Author(s) 2026. CC BY 4.0 License.

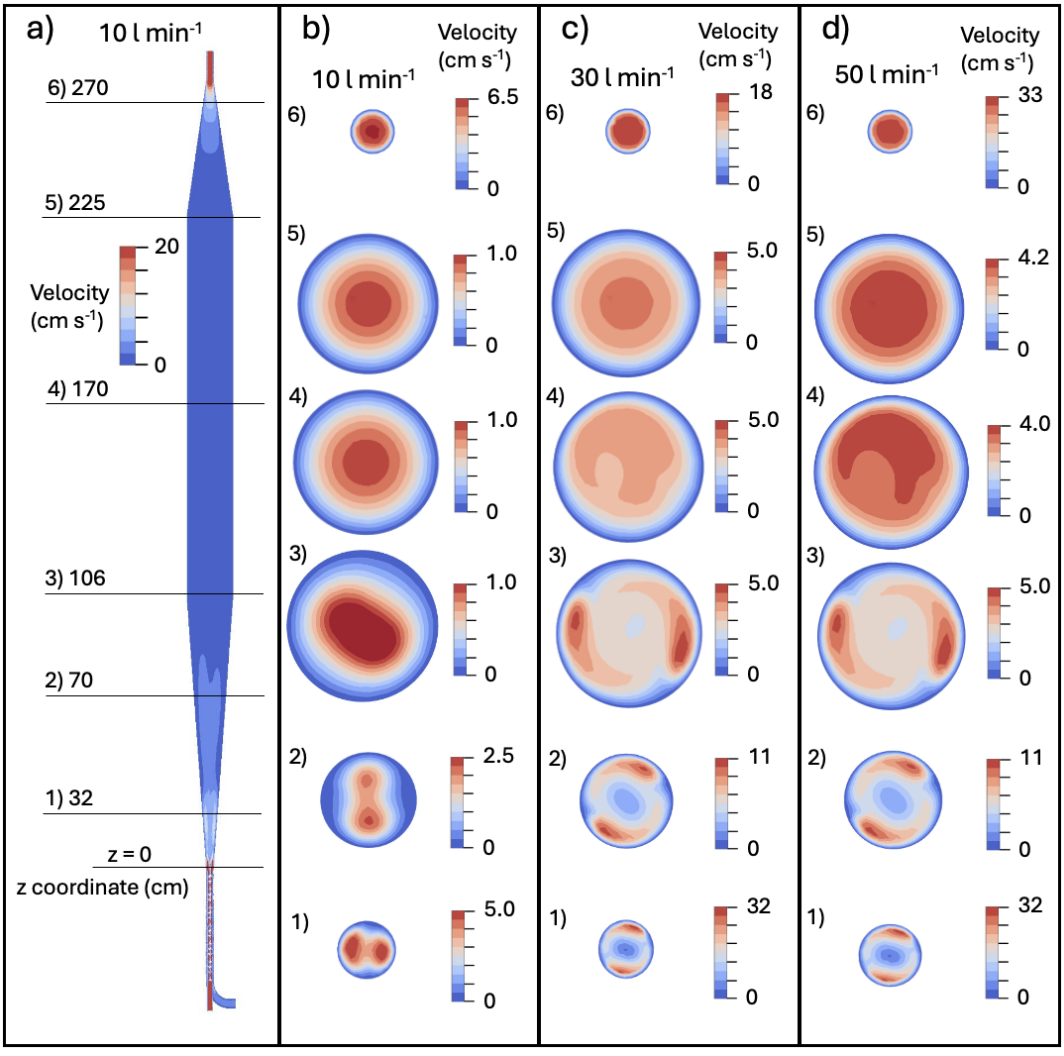


Figure 3. Computational fluid dynamics (CFD) simulation of the FLOTUS flow tube. Panel a) shows the mean velocity versus position along the tube at 10 $\mathrm{L\,min^{-1}}$ flow rate. Panels b)–d) show the total velocity profiles at six transverse sections along the tube, for flow rates of 10, 30 and 50 $\mathrm{L\,min^{-1}}$, respectively. The locations of the transverse sections with respect to the outlet of the static mixer at z = 0 cm are indicated in panel a). The swirling flow created by the static mixer can be seen in the conical entrance section, which settles towards laminar flow further along the flow tube. A control simulation with an imposed 4 $^{\circ}\mathrm{C}$ axial temperature rise between the inlet and the outlet to simulate extreme heating by the UV lamps showed no change in the velocity profiles.

https://doi.org/10.5194/egusphere-2026-6281
Preprint. Discussion started: 4 November 2026
© Author(s) 2026. CC BY 4.0 License.

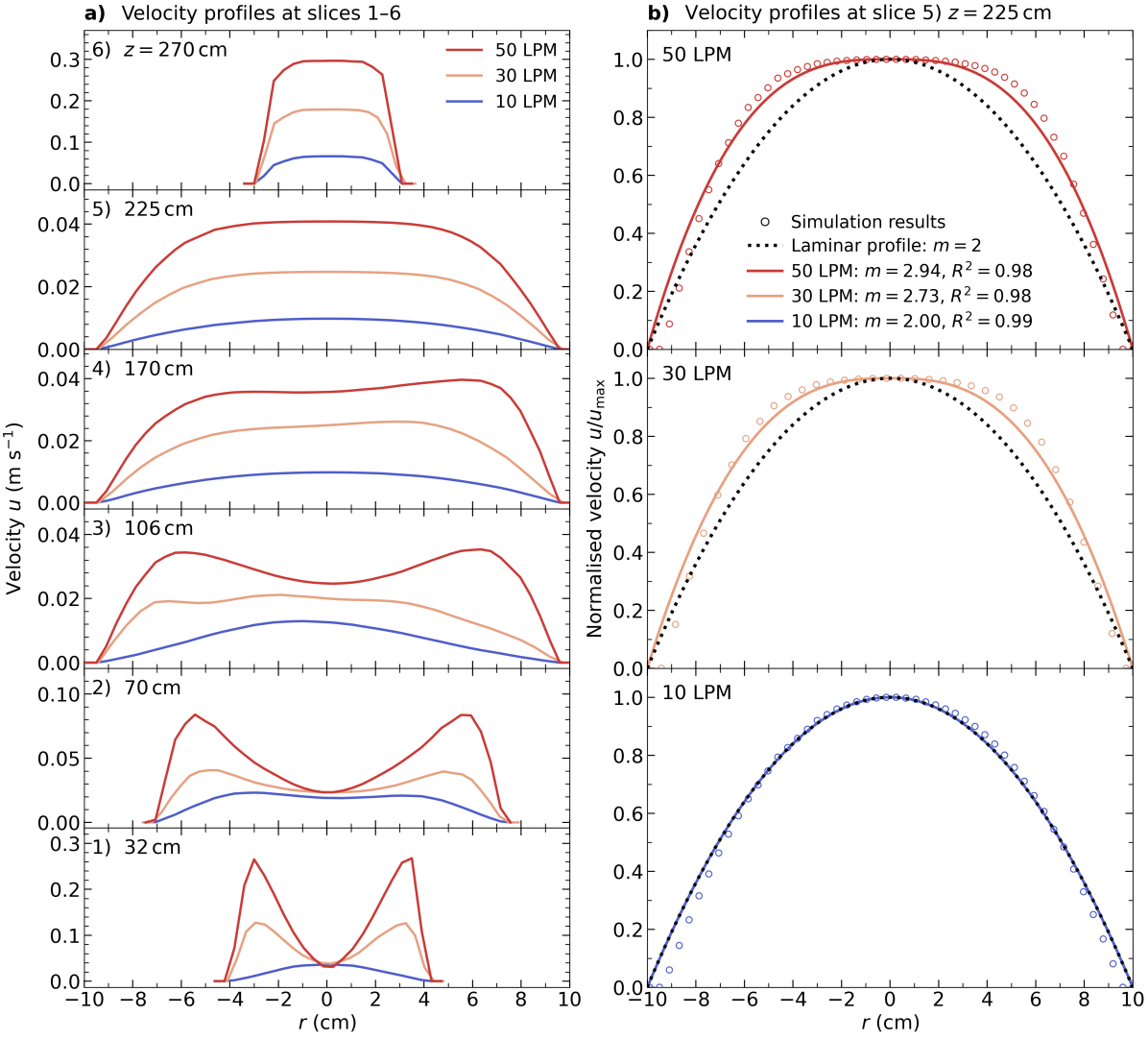


Figure 4. CFD simulations of velocity profiles at various positions along the flow tube. Panel a) shows the velocity profiles versus radial position at each of the six cross sections indicated in Fig. 3a) for three flow rates: 50, 30 and 10 $\mathrm{L\,min^{-1}}$. Panel b) shows the profiles at the end of the cylindrical section (slice 5 at $z = 2.25\,\mathrm{m}$) for each flow rate, normalised by their respective maxima and fitted with Eq. (1). The dotted line shows a laminar (parabolic) reference flow with $m = 2$.

$m > 2$, indicating a flatter velocity profile as the boundary layer develops inwards. The fitted values are 2.00 at 10 $\mathrm{L\,min^{-1}}$, 2.73 at 30 $\mathrm{L\,min^{-1}}$ and 2.94 at 50 $\mathrm{L\,min^{-1}}$, indicating that higher flow rates are not quite fully developed and exhibit a more plug-flow-like behaviour (see Section 4.1).

https://doi.org/10.5194/egusphere-2026-6281
Preprint. Discussion started: 4 November 2026
© Author(s) 2026. CC BY 4.0 License.

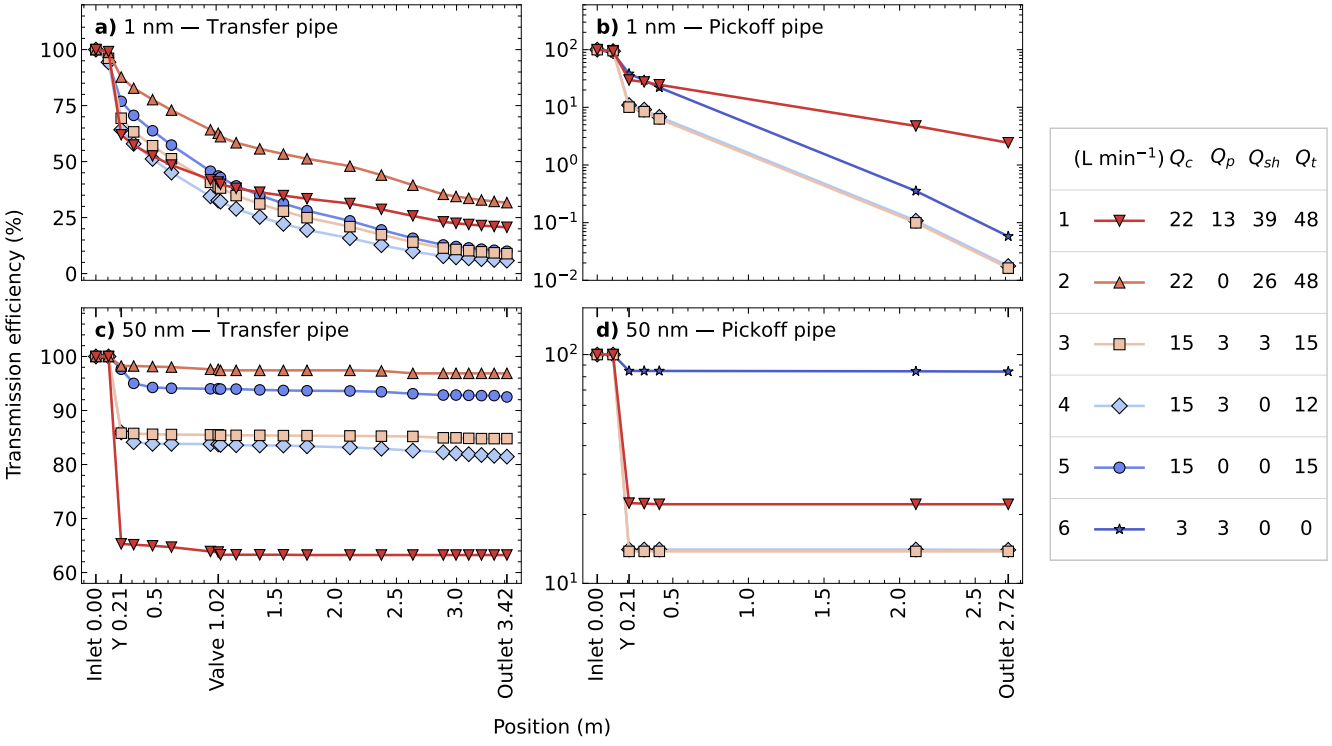


Figure 5. CFD simulations of particle transmission efficiencies through the transfer and pickoff pipes. Panels a) and b) show the transmission efficiencies of 1 nm particles along the transfer and pickoff pipes, respectively. The transmission efficiencies for 50 nm particles are shown in panels c) and d). The different conditions for the core flow Q_c, pickoff flow Q_p, added sheath flow Q_{sh}, and flow transferred to CLOUD Q_t are shown in the legend for each simulation.

3.2 Transmission efficiencies

In a separate set of CFD simulations, we evaluated the transport of 1 nm and 50 nm particles from the FLOTUS core outlet through the transfer and pickoff pipes. Here we simulated the three-dimensional airflow using COMSOL Multiphysics (version 6.0; COMSOL AB, Stockholm, Sweden) (COMSOL AB, 2021) with the Laminar Flow interface under stationary conditions. The working fluid was air, with density and dynamic viscosity obtained from the built-in Air material. Fully developed volumetric-flow conditions were prescribed at all active inlets and outlets, whereas closed ports and the remaining solid surfaces were treated as no-slip walls; a pointwise pressure constraint of 0 Pa was applied adjacent to the downstream outlet to remove the pressure null space. A common hybrid unstructured mesh containing 5,353,981 volume elements (3,829,217 tetrahedra, 1,519,226 prisms, and 5,538 pyramids) and 1,466,588 vertices was used for all configurations, resulting in approximately 5.87 million solved degrees of freedom.

We evaluated different combinations of the core outflow rate Q_c, the flow rate through the pickoff Q_p, the sheath flow rate added to the FLOTUS-to-CLOUD transfer pipe Q_{sh}, and the flow rate transferred into the CLOUD chamber Q_t. We used

https://doi.org/10.5194/egusphere-2026-6281
Preprint. Discussion started: 4 November 2026
© Author(s) 2026. CC BY 4.0 License.

particle trajectory simulations to examine the transmission of 1 nm and 50 nm particles through the FLOTUS transfer system under various flow configurations. All vapours and particles are assumed to be 100% sticky, meaning a single contact with a wall results in loss. The 1 nm particles represent sticky molecules and 50 nm particles represent CCN. Fig. 5a) and 5b) show the transmission efficiencies for 1 nm particles through the FLOTUS-to-CLOUD transfer and the pickoff pipes, respectively. Panels c) and d) show the corresponding transmission efficiencies for 50 nm particles. The different flow configurations are listed in the legend. The overall transmission efficiencies from the core flow exit of FLOTUS to the exit of each pipe are summarised in Table 1.

Table 1. Transmission efficiencies for different flow configurations. Listed are the core flow Q_c, the pickoff flow Q_p, the sheath flow added to the transmission pipe Q_{sh}, and the flow transmitted to CLOUD Q_t. The transmission efficiencies are given separately for 1 nm and 50 nm particles.

Flow rates ($\mathrm{L\,min^{-1}}$)				Transmission to CLOUD (%)		Transmission to pickoff (%)	
Q_c	Q_p	Q_{sh}	Q_t	1 nm	50 nm	1 nm	50 nm
22	13	39	48	20.7	63.2	2.43	22.2
22	0	26	48	31.7	96.9	off	off
15	3	3	15	8.9	84.8	0.0163	13.8
15	3	0	12	5.8	81.5	0.0177	14.0
15	0	0	15	10.0	92.5	off	off
3	3	0	0	off	off	0.0579	84.2

For all flow configurations, 50 nm particles are efficiently transported; they divide into the pickoff and transfer pipes approximately according to their relative flow rates, and the total loss at the Y split and on the walls of the pipes is less than 15 % (Table 1). Due to their high mobility, the transmission efficiency of 1 nm particles is lower. The highest simulated transmission efficiency of 1 nm particle into the CLOUD chamber is 31.7 % for a high total flow rate Q_t = 48 $\mathrm{L\,min^{-1}}$, which nevertheless (just) preserves laminar flow. This is excellent performance considering the length of the transfer pipe (3.42 m) and the presence of two 90° bends plus a gate valve. Lower Q_t values result in lower transmission efficiencies, e.g. 10.0 % at Q_t = 15 $\mathrm{L\,min^{-1}}$ (Table 1). This shows that, to maximise the transfer efficiency of sticky vapours into CLOUD, the pickoff flow should be zero and, for any chosen value the core flow from FLOTUS, sufficient sheath air (Q_sh) should be added to bring Q_t up to 48 $\mathrm{L\,min^{-1}}$.

For transmission of 1 nm particles along the pickoff pipe, all the simulations at Q_p = 3 $\mathrm{L\,min^{-1}}$ have very low transmission efficiency because they are well below the laminar flow rate limit of 13 $\mathrm{L\,min^{-1}}$ for a 9.4 mm ID pipe (Table 1). However, the transmission efficiency is 2.43 % at Q_p = 13 $\mathrm{L\,min^{-1}}$. After approximately accounting for the Y-split ratio, $Q_\mathrm{p}/(Q_\mathrm{p}+Q_\mathrm{t})$ = 13 / (13 + 48) = 0.21, this indicates an overall transmission efficiency for 1 nm particles of 2.43/0.21 = 12 % between the core flow from FLOTUS and the exit of the 2.51 m pickoff pipe, which is good performance. Once again, to maximise the pickoff

https://doi.org/10.5194/egusphere-2026-6281
Preprint. Discussion started: 4 November 2026
© Author(s) 2026. CC BY 4.0 License.

signal requires a flow rate near to the laminar flow limit (Q_p = 13 $\mathrm{L\,min^{-1}}$) and, in this case, for the flow to the CLOUD chamber to be shut off. The value of Q_p is controlled by the mass flow controller (MFC), valve and pump of the analysing instrument.

4 FLOTUS performance

4.1 Gas residence time

4.1.1 Axially dispersed plug flow reactor (AD-PFR) model

A residence-time distribution (RTD) describes the distribution of times spent by fluid elements inside a reactor before they exit (Danckwerts, 1995; Levenspiel, 1999). For a short pulse of a non-reactive tracer, the concentration measured at the outlet is proportional to the RTD. After baseline correction and normalisation, the RTD can be written as

$$E(t) = \frac{C_\mathrm{tr}(t)}{\int_0^\infty C_\mathrm{tr}(t')\,\mathrm{d}t'}, \tag{2}$$

where $C_\mathrm{tr}(t)$ is the measured tracer concentration. For an ideal plug-flow reactor, all fluid elements travel through the reactor at the same velocity and therefore have the same residence time. An instantaneous tracer pulse then exits as an instantaneous pulse delayed by the nominal residence time

$$E_\mathrm{PFR}(t) = \delta\left(t - \tau_\mathrm{calc}\right), \qquad \tau_\mathrm{calc} = V/Q, \tag{3}$$

where δ is the Dirac delta function, τ_{calc}, the mean residence time, V the reactor volume and Q the total flow rate. In practice, the measured signal has a finite width because the injection and detector have finite response times. Additional broadening results from differences in the transport times of fluid elements and therefore a departure from ideal plug flow (Danckwerts, 1995). For comparison, a fully developed laminar velocity profile in a cylindrical tube has a centreline velocity twice the mean velocity across the full cross section. The earliest fluid along the centre of the tube therefore reaches the exit at time $\tau_\mathrm{calc}/2$, while slower fluid closer to the tube wall arrives later, giving rise to a long tail in the RTD (Taylor, 1953).

We quantify the broadening of the tracer pulse with a one-dimensional axially dispersed plug-flow-reactor (AD-PFR) model (Levenspiel, 1999; Huang and Seinfeld, 2019). The model represents the cross-sectionally averaged tracer concentration $C(z,t)$ using a mean convective velocity u and an effective axial dispersion coefficient D_ax,

$$\frac{\partial C}{\partial t} + u\frac{\partial C}{\partial z} = D_\mathrm{ax}\frac{\partial^2 C}{\partial z^2}. \tag{4}$$

The convective term translates the pulse through the reactor, while the dispersion term broadens the pulse in the axial direction. The coefficient D_ax is an effective transport parameter that represents the combined influence of the velocity profile, reactor geometry, radial mixing, and other non-ideal transport processes.

https://doi.org/10.5194/egusphere-2026-6281
Preprint. Discussion started: 4 November 2026
© Author(s) 2026. CC BY 4.0 License.

The relative importance of convection and axial dispersion is expressed by the dimensionless Péclet number,

$$\mathrm{Pe} = \frac{Lu}{D_{\mathrm{ax}}} = \frac{L^2}{D_{\mathrm{ax}}\tau_r}, \tag{5}$$

where L is the reactor length and $\tau_r = L/\bar{u}$ is the fitted residence time (Levenspiel, 1999; Huang and Seinfeld, 2019). This definition compares the characteristic convective transport rate $L\bar{u}$ with the axial dispersion coefficient D_{ax}. A large Pe corresponds to weak relative axial dispersion and a narrow distribution, whereas a small Pe corresponds to stronger dispersion and a broader distribution. In the limit $\mathrm{Pe} \to \infty$, the AD-PFR approaches ideal plug flow. The quantity,

$$\frac{D_{\mathrm{ax}}}{\bar{u}L} = \frac{1}{\mathrm{Pe}}, \tag{6}$$

is the dispersion number, which is used to describe the departure from plug flow in the axial-dispersion model (Levenspiel, 1999; Huang and Seinfeld, 2019).

The main cylindrical section of FLOTUS is $1.336\,\mathrm{m}$ long and has an inner diameter of $0.20\,\mathrm{m}$, while the total internal volume of $60\,\mathrm{L}$ also includes the conical inlet and outlet sections (Fig. 1). Because all three quartz sections are exposed to UV radiation, we represent the complete flow tube by a constant area reactor with the diameter of the main cylindrical section. This gives the volume-equivalent reactor length $L_{\mathrm{eq}} = V/A = 1.910\,\mathrm{m}$, where $A = \pi r^2$ and $r = 0.10\,\mathrm{m}$. The quantity L_{eq} is a one-dimensional volume-equivalent length rather than the physical end-to-end length. This definition preserves the nominal residence time, $\tau_{\mathrm{calc}} = L_{\mathrm{eq}}/\bar{u}_{\mathrm{calc}} = V/Q$, where $\bar{u}_{\mathrm{calc}} = Q/A$.

For an instantaneous inlet pulse, the AD-PFR transport equation has an analytical outlet response that can be written in dimensionless form as

$$E_{\mathrm{pulse}}(\theta) = \sqrt{\frac{\mathrm{Pe}}{4\pi\theta}} \exp\left[-\frac{(1-\theta)^2}{4\theta/\mathrm{Pe}}\right], \tag{7}$$

where $\theta = t/\tau_r$ is dimensionless time (Huang and Seinfeld, 2019). The fitted residence time τ_r determines the time scale and position of the response, while Pe determines its width. Increasing Pe therefore produces a narrower response that approaches the ideal plug-flow limit. We fit Eq. 7 to each mean tracer response, using τ_r and D_{ax} as free parameters. The Péclet number and its uncertainty are then calculated from the fitted parameters using Eq. 5.

4.1.2 Gas residence time measurements

We measure the residence-time distribution in FLOTUS by injecting short pulses of toluene and measuring their arrival time and intensity profile with an H_3O^+-PTR-MS (STOF) (Graus et al., 2011; Canaval et al., 2019) connected to the pickoff pipe. We first filled the toluene injection line from a cylinder containing $1000\,\mathrm{ppm}$ toluene in N_2, while the injection valve to FLOTUS remained closed. We then closed the cylinder valve once the line had been pressurised, and opened the FLOTUS valve. This procedure rapidly released a short burst of pressurised gas from the line into FLOTUS. Because the burst duration was around one second, we treat the injection as an instantaneous pulse. The STOF samples at the pickoff with a time resolution of $1\,\mathrm{s}$.

Figure 6 shows the measured RTDs for total flow rates of 15, 25, 30, and $45\,\mathrm{L\,min^{-1}}$ (all include $1\,\mathrm{L\,min^{-1}}$ of sheath in flow). All experiments were conducted at a FLOTUS temperature of $+5\,^{\circ}\mathrm{C}$. The individual experiments are shown as grey

https://doi.org/10.5194/egusphere-2026-6281
Preprint. Discussion started: 4 November 2026
© Author(s) 2026. CC BY 4.0 License.

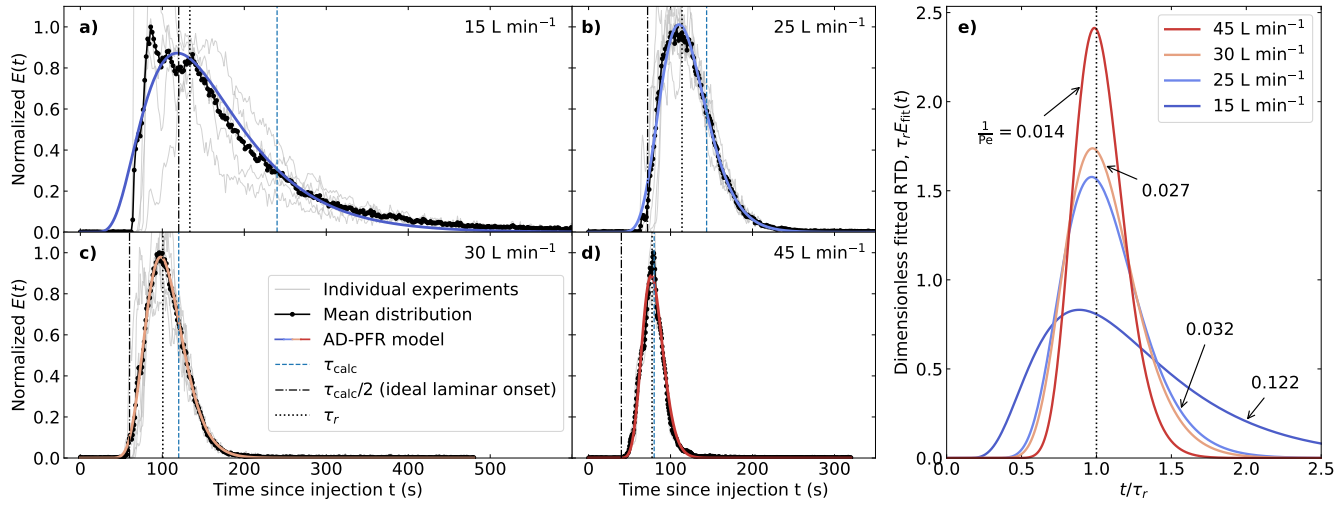


Figure 6. Residence-time distributions of toluene pulses. Panels a)-d) show individual experiments in grey, with their mean values shown in black circles, for total flows of 15, 25, 30, and 45 L min^{-1}. The coloured curves show the fits of the Axially Dispersed Plug Flow Reactor (AD-PFR) model (Huang and Seinfeld, 2019) and the vertical dotted lines shows the fitted mean residence times τ_r. The vertical blue dashed lines show the calculated mean residence time $\tau_{\mathrm{calc}} = V/Q$ and the dash-dotted line shows $\tau_{\mathrm{calc}}/2$ (the leading-edge time expected for a fully developed laminar flow). Panel e) shows the four AD-PFR fits plotted versus dimensionless time, t/τ_r, with annotations indicating the dispersion number $1/\mathrm{Pe} = D_{\mathrm{ax}}/(\bar{u}L)$. All experiments were conducted at a FLOTUS temperature of +5 °C.

Table 2. Axially dispersed plug flow reactor (AD-PFR) fits to the measured residence-time distributions in Fig. 6. Shown are the FLOTUS total flow rate Q, the number of experiments in each averaged distribution N, the calculated residence time τ_{calc}, and the fitted values for residence time τ_r, axial dispersion coefficient D_{ax}, Péclet number Pe and coefficient of determination R^2. The uncertainties are one standard deviation of the fit. The uncertainty of Pe is propagated from the fitted parameters.

Q (L min^{-1})	N	τ_{calc} (s)	τ_r (s)	D_{ax} (m^2 s^{-1})	Pe	R^2
15	5	240	133.60 ± 0.70	$(3.34 \pm 0.07) \cdot 10^{-3}$	8.2 ± 0.2	0.954
25	6	144	113.99 ± 0.13	$(1.040 \pm 0.008) \cdot 10^{-3}$	30.8 ± 0.2	0.994
30	6	120	100.61 ± 0.06	$(9.68 \pm 0.04) \cdot 10^{-4}$	37.5 ± 0.2	0.998
45	2	80	77.46 ± 0.09	$(6.47 \pm 0.07) \cdot 10^{-4}$	72.7 ± 0.8	0.986

lines in Figs. 6a)–d), and their mean distributions at each flow rate as solid black points. The coloured lines in Figs. 6a)–e) show the fits to the data of the AD-PFR model (Eq. 7), and the fitted values of the parameters are summarised in Table 2.

Figure 6e) overlays the fitted distributions in dimensionless form. The dispersion number $D_{\mathrm{ax}}/(\bar{u}L) = 1/\mathrm{Pe}$ decreases from 0.122 at 15 L min^{-1} to 0.032, 0.027, and 0.014 at 25, 30, and 45 L min^{-1}, respectively. These values can be directly compared to the dimensionless tracer-response curves shown in Levenspiel (1999) and show good agreement: the 45 L min^{-1} case lies close to the small-dispersion limit of $D_{\mathrm{ax}}/(\bar{u}L) = 0.01$, the 25 and 30 L min^{-1} cases lie between the 0.02 and 0.05 reference

https://doi.org/10.5194/egusphere-2026-6281
Preprint. Discussion started: 4 November 2026
© Author(s) 2026. CC BY 4.0 License.

curves, and the $15\,\mathrm{L\,min^{-1}}$ case is close to the substantially broader curve at $D_{\mathrm{ax}}/(\bar{u}L) = 0.1$. The broad tail at $15\,\mathrm{L\,min^{-1}}$ therefore represents the strongest departure from plug flow behaviour (and approach to fully developed laminar flow), while increasing the flow progressively shifts FLOTUS towards ideal plug flow. The fitted τ_r also approaches τ_{calc} as the flow increases. We see from Figs. 6a)–d), that the residence time distributions narrow as well as shorten as the total flow increases, while the fitted Péclet numbers decrease from 72.7 at $45\,\mathrm{L\,min^{-1}}$ to 8.2 at $15\,\mathrm{L\,min^{-1}}$, reflecting a fully developed laminar flow at the lowest flow rate. The high quality of the fits to the AD-PFR model and the values of the fitted Péclet numbers indicate that bulk transport of molecules dominates over diffusion and turbulence in FLOTUS at all these flow rates.

4.2 Hydroxyl (OH) radicals

4.2.1 Hydroxyl radical exposure

The essential function of oxidation flow reactors (OFRs) is to provide highly elevated concentrations of atmospheric oxidants, in particular hydroxyl (OH) radicals, over their short residence times so that vapours can receive an exposure equivalent to several days in the ambient atmosphere. The OH exposure ($\mathrm{cm^{-3}s}$) is defined by

$$\mathrm{OH_{exp}} = \int [\mathrm{OH}](t)\,\mathrm{d}t, \tag{8}$$

which can be expressed as an atmospheric-equivalent oxidation time using a representative atmospheric OH concentration of around $10^6\ \mathrm{cm^{-3}}$ (Kang et al., 2007; Lambe et al., 2011; Huang et al., 2017). Flow reactors can, therefore, be used to simulate atmospheric-equivalent oxidative processing on gas-phase precursors and aerosol particles over practical timescales in the laboratory. However, the high oxidant concentrations and short residence times can also lead to reaction pathways that differ from those in the atmosphere (Kang et al., 2007; Lambe et al., 2011).

Oxidation by OH radicals changes the gas composition and volatility distribution by reacting away the precursor and forming reaction products, thereby affecting the formation rates, growth rates, and chemical composition of the resulting aerosol particles. The OH exposure consequently measures the extent of the oxidation imposed by FLOTUS before the particles are introduced into CLOUD. FLOTUS generates OH radicals from ozone and water vapour under intense 254 nm UV illumination by the reactions

$$\mathrm{O_3} + h\nu\,(254\,\mathrm{nm}) \rightarrow \mathrm{O_2} + \mathrm{O(^1D)} \tag{9}$$

$$\mathrm{O(^1D)} + \mathrm{H_2O} \rightarrow 2\mathrm{OH}. \tag{10}$$

The fraction of $\mathrm{O(^1D)}$ that reacts with water vapour rather than being collisionally quenched by air molecules depends on the water vapour concentration. The resulting OH concentration is therefore controlled by the photon flux, $\mathrm{O_3}$ concentration, and water vapour concentration, as well as by subsequent radical recycling and reactions with the other trace gases in the reactor (Peng et al., 2015). Ozone is also a rapid oxidant of organic compounds with double bonds, so $\mathrm{OH_{exp}}$ describes only the hydroxyl component of the oxidation history rather than the total oxidant exposure.

https://doi.org/10.5194/egusphere-2026-6281
Preprint. Discussion started: 4 November 2026
© Author(s) 2026. CC BY 4.0 License.

We determine the OH exposure from the change in the steady-state toluene concentration under UV illumination. The loss of toluene through reaction with OH is described by

$$\frac{\mathrm{d[Tol]}}{\mathrm{d}t} = -k_{\mathrm{OH+Tol}}(T)[\mathrm{OH}](t)[\mathrm{Tol}], \tag{11}$$

where t represents the reaction time along the reactor. We use the temperature-dependent rate coefficient $k_{\mathrm{OH+Tol}}(T) = 1.8 \cdot 10^{-12} \exp(340/T)\,\mathrm{cm^3\,molecule^{-1}\,s^{-1}}$ recommended for 210–350 K by Mellouki et al. (2021). The corresponding OH exposure is then

$$\int_0^{\tau_r} [\mathrm{OH}](t)\,\mathrm{d}t = \frac{\ln\left([\mathrm{Tol}]_{\mathrm{dark}}/[\mathrm{Tol}]_{\mathrm{light}}\right)}{k_{\mathrm{OH+Tol}}(T)}, \tag{12}$$

where τ_r is the residence time in FLOTUS and $[\mathrm{Tol}]_{\mathrm{dark}}$ and $[\mathrm{Tol}]_{\mathrm{light}}$ are the steady-state toluene concentrations measured at the reactor outlet with the UV lamps off and on, respectively. This calculation assumes that the lamp-induced change in toluene is dominated by its reaction with OH and that other toluene losses do not change between the dark and illuminated steady states. For these experiments, the only other significant toluene loss is through dilution, i.e. passage out of FLOTUS.

4.2.2 Hydroxyl radical measurements

We show in Fig. 7 an example toluene attenuation experiment to measure OH exposure in FLOTUS, together with a detailed description in the caption.

Figure 8 shows a set of experiments in which we measured the toluene-derived OH exposures under different operating conditions. Panel a) shows OH exposure vs number of illuminated lamps at otherwise unchanged conditions of $30\,\mathrm{L\,min^{-1}}$ total flow, $+5\,^{\circ}\mathrm{C}$, and $[\mathrm{H_2O}] = 1.1 \cdot 10^{17}\,\mathrm{cm^{-3}}$. Panel a) shows that the OH exposure increases linearly with the number of illuminated lamps, demonstrating that each lamp provides comparable illumination of FLOTUS and that the oxidative conditions in FLOTUS can be controlled by the number of lamps in operation. In addition to the lamp intensity, the OH exposure depends strongly on the water-vapour concentration (Fig. 8b). These features are consistent with OH production by photolysis of $\mathrm{O_3}$ at 254 nm and the subsequent reaction of $\mathrm{O(^1D)}$ with $\mathrm{H_2O}$. All experiments shown in Fig. 8 were conducted at dark $\mathrm{O_3}$ concentrations between 180 and 220 ppb. Together, these measurements demonstrate that the OH exposure in FLOTUS can be varied over a broad range by adjusting the lamp number and water-vapour concentration as well as ozone concentration (which was not tested).

In these experiments, we measure OH exposures of up to $3 \cdot 10^{11}\,\mathrm{cm^{-3}\,s}$. The mean residence time, τ_r, at a total flow of $30\,\mathrm{L\,min^{-1}}$ is around 100 s (Table 2). This corresponds to an average OH concentration of $3 \cdot 10^{9}\,\mathrm{cm^{-3}}$, as indicated on the right-hand vertical axes in Fig. 8. For comparison with atmospheric oxidation, Lambe et al. (2011) express OH exposure as an equivalent photochemical age using a representative 24-h average atmospheric OH concentration of $1.5 \cdot 10^{6}\,\mathrm{cm^{-3}}$ (an OH exposure of $1.3 \cdot 10^{11}$ $\mathrm{cm^{-3}s}$). Using this value, an OH exposure of $3 \cdot 10^{11}\,\mathrm{cm^{-3}\,s}$ corresponds to approximately 2.3 days of equivalent atmospheric OH exposure. Even higher OH exposures can be reached in FLOTUS by increasing the $\mathrm{O_3}$ concentration or else the $\mathrm{H_2O}$ concentration, either by increasing the relative humidity at a given temperature or by operating at warmer temperature at the same relative humidity.

https://doi.org/10.5194/egusphere-2026-6281
Preprint. Discussion started: 4 November 2026
© Author(s) 2026. CC BY 4.0 License.

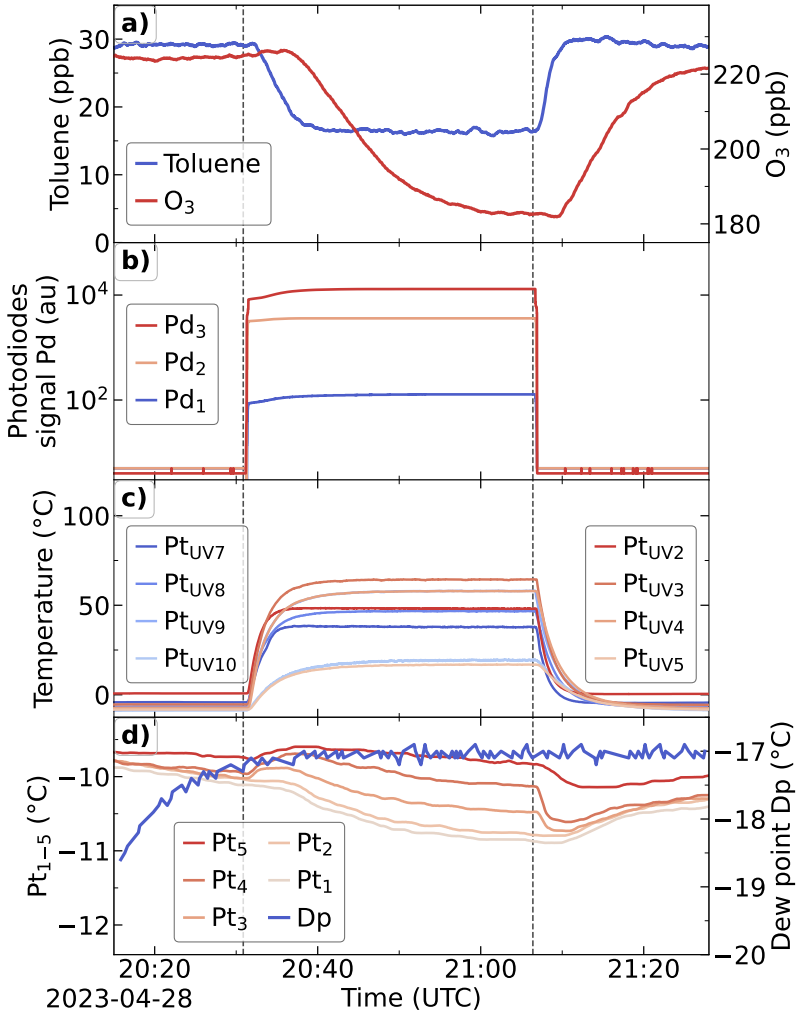


Figure 7. Example experiment to measure OH exposure in FLOTUS. Before the start of the experiment, steady conditions are established for toluene, ozone, relative humidity (dewpoint) and temperature. The vertical dashed lines indicate when all six UV lamps were switched on around 20:30 and then off around 21:10. Panel a) shows the concentrations of toluene and O_3 measured at the exit of FLOTUS. The reduction of toluene when the lights are on results from the additional loss rate due to oxidation by OH radicals. The slow response of the ozone measurement does not indicate the true time development but is due to sampling from the sheath air out flow, and the sampling line includes large buffer volumes. Panel b) shows the photodiode (PD) responses; there is a small variation near the start as the lamps warm up to their stable temperature. Panel c) shows the UV lamp temperatures. Panel d) shows the FLOTUS dew point (DP) as well as the temperatures from the bottom to the top of the FLOTUS thermal housing. The thermoregulator rapidly senses the additional heat load when the lamps are switched on and tries to maintain Pt_5 close to the setpoint near -9.6 °C. The locations of the photo-diode and temperature sensors are shown in Fig. 1b). At full lamp power, the difference in temperature between the top and bottom of the FLOTUS is around 1 °C. For this experiment, the total flow through FLOTUS was 30 $\mathrm{L\,min^{-1}}$.

https://doi.org/10.5194/egusphere-2026-6281
Preprint. Discussion started: 4 November 2026
© Author(s) 2026. CC BY 4.0 License.

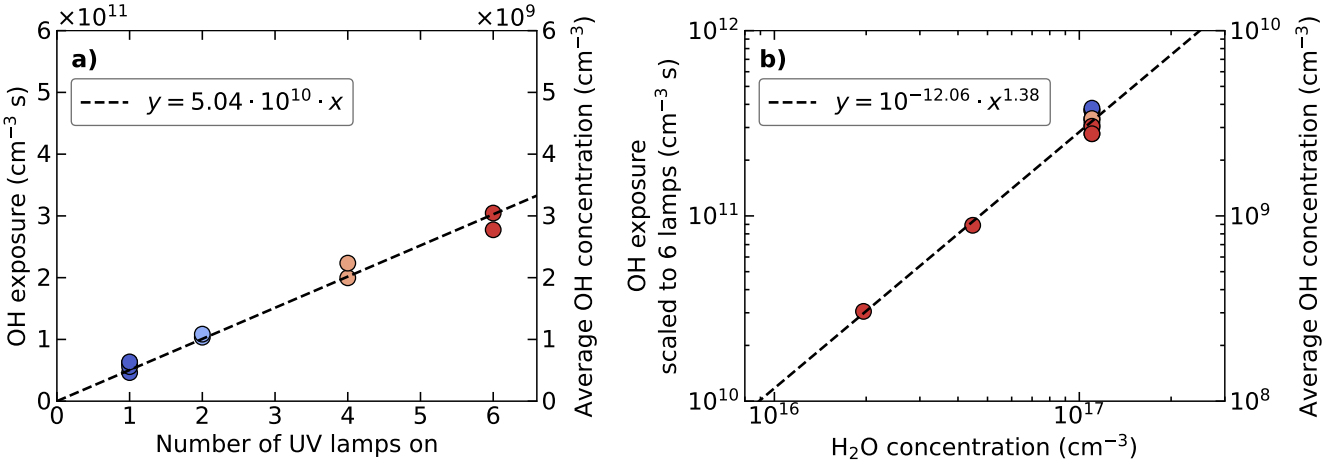


Figure 8. OH exposure measurements from toluene attenuation experiments. Panel a) shows measurements of the OH exposure and resulting average OH concentration in FLOTUS versus number of illuminated UV lamps, at a fixed H_2O concentration of $1.1 \cdot 10^{17}$ cm^{-3} and 5 °C temperature. The abscissa and symbol colour indicate how many lamps were illuminated. A linear fit through the data is shown by the dashed line. Panel b) shows the OH exposure and average OH concentration versus H_2O concentration. Here, all measurements are simply scaled up to 6 lamps to determine the OH exposure, and a power law fit is shown as a dashed line. The experimental conditions are 180–220 ppbv O_3, 10–30 ppbv toluene and a FLOTUS total flow of 30 L min^{-1}. The FLOTUS temperature range for panel b) is -22 °C to +5 °C.

4.3 Aerosol particles

4.3.1 Particle size distributions

FLOTUS offers several experimental handles for generating different aerosol particle size distributions. The precursor system and its concentrations determine the condensable vapours and the resulting particle composition. The total flow rate controls the residence time; decreasing the flow rate increases the time available for growth by coagulation and condensation, and decreases the final particle number. The OH exposure can be tuned by changing the O_3 and water vapour concentrations, as well as the UV photon flux. The positions of the UV lamps also determine where along the reactor the OH is produced, thereby changing the spatial exposure profile, even though the integrated OH exposure does not depend on which lamp is illuminated. Temperature and humidity affect reaction kinetics, vapour saturation pressures, aerosol water content, and gas-particle partitioning, which in turn influence the balance between nucleation and growth. Their effect on particle size is therefore system-dependent and does not have a universal direction. Together, these controls provide great flexibility for FLOTUS to generate particles spanning a wide range of sizes, chemical compositions and oxidation states.

As shown in Fig. 9, we use several precursor systems to demonstrate the range of aerosol particles that FLOTUS can produce. The geometric mean diameters of the particles range from 8 to 136 nm. Note that these distributions shown should be seen as examples. A given particle size is not uniquely associated with one precursor system, and similar range of sizes as shown

https://doi.org/10.5194/egusphere-2026-6281
Preprint. Discussion started: 4 November 2026
© Author(s) 2026. CC BY 4.0 License.

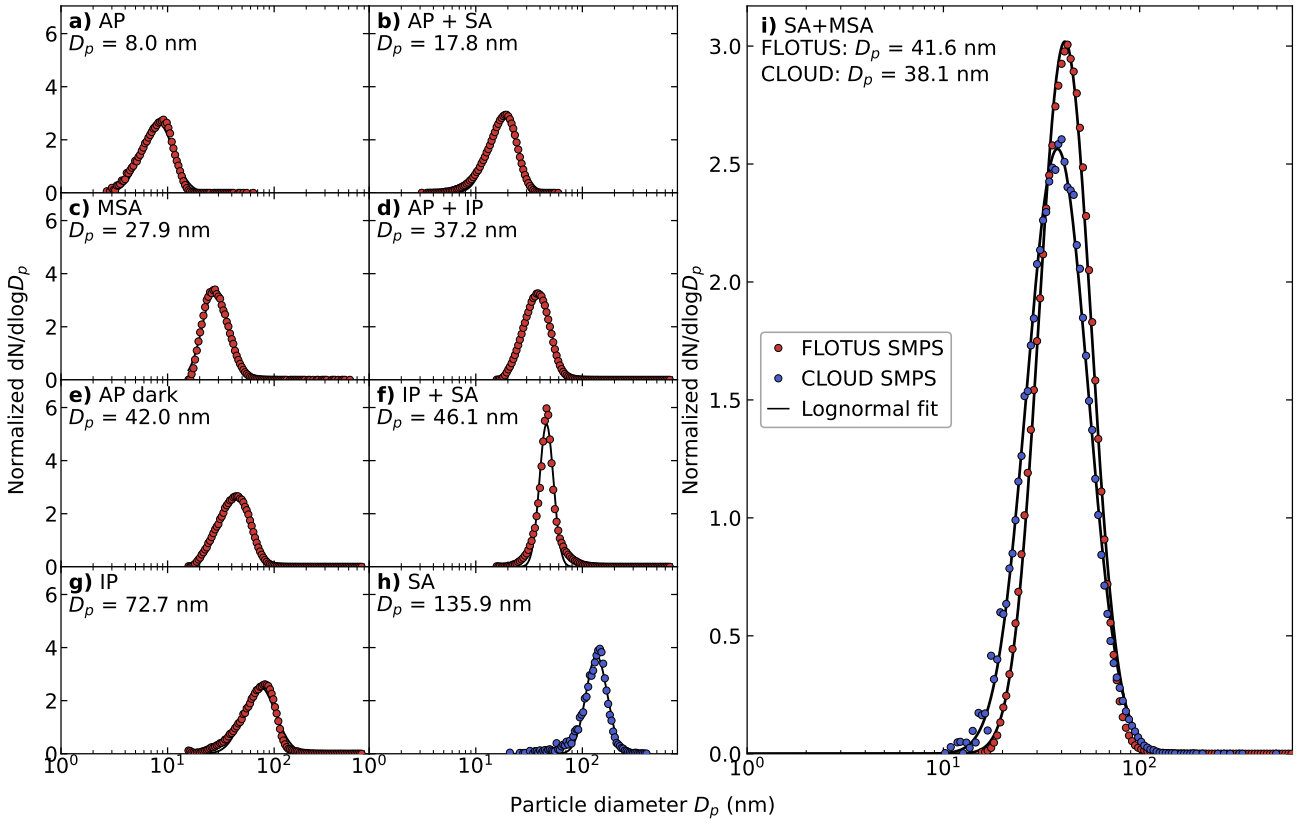


Figure 9. Particle number size distributions produced by FLOTUS from different precursors. The panels show particle size distributions produced by a) α-pinene (AP), b) AP + sulfuric acid (SA), c) methanesulfonic acid (MSA), d) AP + isoprene (IP), e) AP without UV illumination, f) IP + SA, g) IP and h) SA. The panels are arranged by increasing geometric mean diameter, as shown in the annotations. Panel i) shows the size distributions for particles made from SA and MSA measured simultaneously at the FLOTUS pickoff pipe (red) and after injection into the CLOUD chamber (blue). Each distribution in panels a) to i) is normalised by its integrated number concentration over the measured size range. Panels a) and b) are measured with an nSMPS, and panels c) to g), as well as the red circles in panel i), are measured with an lSMPS connected to the pickoff pipe. Panel (h) and the blue circles in panel i) show a measurement with an lSMPS after injection into the CLOUD chamber. The black curves show single-mode log-normal fits to each distribution. A list of the fitted parameters, FLOTUS operating conditions and precursor concentrations is provided in Table 3.

https://doi.org/10.5194/egusphere-2026-6281
Preprint. Discussion started: 4 November 2026
© Author(s) 2026. CC BY 4.0 License.

Table 3. Lognormal-fit results, physical operating conditions, and estimated trace-gas mixing ratios for the size distributions in Fig. 9. D_g is the geometric mean diameter, σ_g is the geometric standard deviation, and R^2 is the coefficient of determination of the lognormal fit. Q_F is the total FLOTUS flow, and T_F is the FLOTUS temperature. The dew-point temperature T_{DP}, as well as the O_3 concentration, are measured from the sheath-air outflow. The unreacted concentrations of trace gases (α-pinene (AP), isoprene (IP), SO_2, and methanesulfonic acid (MSA)) are estimated from the mass flow controller settings in the gas system. The conditions in the CLOUD chamber for panel i) are 7.3 °C dewpoint and 15.0 °C temperature.

		Lognormal fit			FLOTUS operating conditions					Trace gases (ppbv)			
Panel	System	D_g (nm)	σ_g	R^2	Q_F (L min^{-1})	T_F (°C)	T_{DP} (°C)	UV lamp ID	O_3 (ppbv)	AP	IP	SO_2	MSA
a)	AP	8.0	1.41	0.972	72.2	29.7	2.4	3	598	7	0	0	0
b)	AP + SA	17.8	1.37	0.980	48.1	29.6	-0.8	3, 6	771	11	0	0.5	0
c)	MSA	27.9	1.31	0.990	10.4	15.4	7.1	dark	0	0	0	0	5.4
d)	AP + IP	37.2	1.33	0.997	17.2	29.3	4.8	1	755	30	118	0	0
e)	AP dark	42.0	1.41	0.993	17.3	28.0	10.0	dark	1989	30	0	0	0
f)	IP + SA	46.1	1.16	0.975	17.3	28.6	4.5	1	1911	0	116	10	0
g)	IP	72.7	1.41	0.964	17.2	29.9	9.8	1	388	0	585	0	0
h)	SA	135.9	1.26	0.973	13.1	40.5	4.2	1, 4	257	0	0	115	0
i) FLOTUS	SA + MSA	41.6	1.36	0.998	9.6	15.4	8.1	1	76	0	0	0.7	0.74
i) CLOUD		38.1	1.43	0.997									

here can be generated for any of these chemical systems (and others that are not shown). Most of the selected distributions in Fig. 9 were generated by UV-induced oxidation of a precursor gas such as SO_2, α-pinene or isoprene. The exceptions are methanesulfonic acid (panel c) and dark ozonolysis of α-pinene (panel e).

Each size distribution was averaged over approximately 10 min. For each selected interval, we average the SMPS measurements in each mobility-diameter bin. We fit the resulting number-size distribution with a single lognormal mode:

$$\frac{\mathrm{d}N}{\mathrm{d}\log_{10} D_p} = \frac{N_{mode}}{\sqrt{2\pi}\log_{10}\sigma_g} \exp\left[-\frac{(\log_{10} D_p - \log_{10} D_g)^2}{2(\log_{10}\sigma_g)^2}\right], \tag{13}$$

where D_p is the electrical-mobility diameter, N_{mode} is the integrated number concentration of the fitted mode, D_g is the geometric mean diameter, and σ_g is the geometric standard deviation.

Figures 9a)–9g) show size distributions measured at the FLOTUS pickoff exit, and Fig. 9h shows the size distribution measured in the CLOUD chamber, after injection from FLOTUS. Figure 9i) compares the SA+MSA size distribution measured at the FLOTUS pickoff (red) and after injection into CLOUD (blue), when the FLOTUS and CLOUD temperatures and dewpoints differ by less than 1 °C. The fitted geometric mean diameters decreases from 41.6 nm at the FLOTUS pickoff to 38.1 nm in CLOUD, and the distribution broadens slightly. The measured small decrease in size may be explained by partial evaporation of MSA from the particle after dilution in CLOUD, which lowers the gas-phase MSA concentration and changes the gas-particle equilibrium. Gas-particle partitioning theory predicts that condensed material can then evaporate from the particle until a new equilibrium is reached (Seinfeld and Pandis, 2016). MSA undergoes condition-dependent gas-particle partitioning, with its effective volatility influenced by temperature, relative humidity, and aerosol acidity or the availability of gas-phase bases (Hodshire et al., 2019; Miljevic et al., 2025).

https://doi.org/10.5194/egusphere-2026-6281
Preprint. Discussion started: 4 November 2026
© Author(s) 2026. CC BY 4.0 License.



4.3.2 Particle injection rates into CLOUD

Table 3 lists the experimental conditions for each of the particle size distributions shown in Fig. 9: chemical system, log-normal fit values, total flow through FLOTUS Q_{F}, temperature T_{F}, dew-point temperature T_{DP}, UV lamps (following the labeling scheme shown in Fig. 1c), ozone concentration and estimated trace-gas mixing ratios. Due to high precursor concentrations in the range 10–600 ppbv (Table 3), the nucleation rates inside FLOTUS are expected to be very high. Under these conditions, the particle number concentrations will be dominated by coagulation losses. Therefore, self preserving, slightly asymmetric particle size distributions, that are close to a lognormal distribution, are expected from FLOTUS with geometric standard deviations in the range 1.3–1.4, characteristic of coagulation-dominated growth (Lee, 1983; Lee et al., 1997; Zhao et al., 2015). The measurements summarised in Table 3 confirm that FLOTUS produces slightly skewed particle size distributions, that are close to a lognormal distribution with geometric standard deviations, σ_{g}, between 1.16 and 1.43 over a wide range of mean geometric diameters, D_{g}, between 8.0 and 136 nm.

Assuming particle losses in FLOTUS are dominated by coagulation, the number concentration after time, t, is given by $N(t) = N_0/(1 + (t/\tau_c))$, where N_0 is the initial particle number concentration and $\tau_c = 2/(k\,N_0)$ is the characteristic time to reduce the initial population by a factor 2 (Seinfeld and Pandis, 2016). Here, k is the collision rate coefficient for equal-sized particles, which is approximately constant and has the value $1.5 \cdot 10^{-9}$ $\mathrm{cm^3 s^{-1}}$ in the 10–100 nm range. The number concentration in FLOTUS is then $N(t) \sim N_0/(1 + 0.5\,k\,N_0\,t)$. For very large N_0 above around 10^9 $\mathrm{cm^{-3}}$, this rapidly reaches a maximum concentration that is independent of the initial (nucleated) particle number concentration, given by $N(t) = 2/k\,t$, where t is the coagulation time in FLOTUS, i.e. the residence time.

We can apply this relationship to the particle population shown in Fig. 9i) to estimate the particle number concentration at the exit of FLOTUS. Here the total flow rate through FLOTUS was Q_F = 9.6 $\mathrm{L\,min^{-1}}$, corresponding to 375 s mean residence time. A combined sampling rate of 2.5 $\mathrm{L\,min^{-1}}$ was taken by the O_3 analyser and dew point monitor via the sheath air out flow. So the core flow entering the transfer pipe was Q_c = 7.1 $\mathrm{L\,min^{-1}}$. The lSMPS connected to the pickoff used a sampling rate of Q_p = 0.3 $\mathrm{L\,min^{-1}}$, so the transfer flow into the CLOUD chamber was Q_t = 6.8 $\mathrm{L\,min^{-1}}$. Assuming coagulation-dominated losses, the particle number concentration at the exit of FLOTUS is then $N(t) = 2/k\,t = 2/(1.5 \cdot 10^{-9} \cdot 375) = 3.6 \cdot 10^6$ $\mathrm{cm^{-3}}$. The flow rate into CLOUD is $6.8 \cdot 1000/60 = 113$ $\mathrm{cm^3 s^{-1}}$. So the predicted particle injection rate into CLOUD is $3.6 \cdot 10^6 \cdot 113 \cdot 0.9 = 3.7 \cdot 10^8$ $\mathrm{s^{-1}}$, where we assume a transfer efficiency of 0.9 (Table 1). This is in good agreement with the particle formation rate of 15 $\mathrm{cm^{-3} s^{-1}}$ measured in the 26.1 $\mathrm{m^3}$ CLOUD chamber during this injection from FLOTUS, which implies a particle injection rate of $2.61 \cdot 10^7 \cdot 15 = 3.9 \cdot 10^8$ $\mathrm{s^{-1}}$.

We can also compare the mass concentrations of particles measured at the pickoff with those measured in CLOUD. Here we use the CLOUD lSMPS time series to determine a mass injection rate from FLOTUS into the CLOUD chamber of 16.1 $\mathrm{ng\,s^{-1}}$, assuming spherical particles with a density of 1 $\mathrm{g\,cm^{-3}}$. In that particular configuration, we measure a mass flux into the FLOTUS lSMPS of 0.724 $\mathrm{ng\,s^{-1}}$. Table 1 shows that the mass transmission efficiency of particles with a $D_g \approx 40$ nm) towards the pickoff is well approximated by the ratio of the pickoff and CLOUD flow rates (Q_p/Q_t), which yields a pickoff transmission efficiency of around 4 % for this configuration. Taking this into account, the total mass flux in FLOTUS is 18.1 $\mathrm{ng\,s^{-1}}$. The

https://doi.org/10.5194/egusphere-2026-6281
Preprint. Discussion started: 4 November 2026
© Author(s) 2026. CC BY 4.0 License.

transfer flow simulation results in Fig. 5c) show that the FLOTUS-to-CLOUD transfer efficiency for large particles increases with decreasing pickoff flow Q_p. The simulation yields a transfer efficiency of above 80 % for $Q_p = 3\,\mathrm{L\,min^{-1}}$ and $> 90\,\%$ for $Q_p = 0$. We therefore conservatively assume a FLOTUS-to-CLOUD transmission efficiency for this configuration with $Q_p = 0.3\,\mathrm{L\,min^{-1}}$ and $Q_t = 6.8\,\mathrm{L\,min^{-1}}$ of at least 90 %. We calculate an expected mass transfer into the CLOUD chamber of $0.9 \cdot 18.1 = 16.3\,\mathrm{ng\,s^{-1}}$, which is in good agreement with the measured value of $16.1\,\mathrm{ng\,s^{-1}}$.

4.4 Aged organic aerosol

4.4.1 Organic aerosol oxygenation state

To measure the organic aerosol oxidation state of particles produced in FLOTUS, we used an Aerosol Mass Spectrometer (HR-ToF-AMS; Aerodyne Research, Inc.; see Sec. 2.4) connected to the pickoff pipe. We performed f_{43}/f_{44} triangle analysis as described in Ng et al. (2010). In brief, f_{43} represents the fraction of organic aerosol associated with $m/z = 43$, dominated by $C_2H_3O^+$, and f_{44} represents the fraction with $m/z = 44$, dominated by CO_2^+. Synthetic air used in FLOTUS does not contain CO_2, so the CO_2^+ contribution from air peaks in the AMS fragmentation table was set to 0 during this analysis. Higher f_{44} values and lower f_{43} values are associated with more highly oxidized aerosol and different oxygenated functional groups. The two fractions are calculated from the organic signals at their respective m/z values

$$f_{43} = \frac{\mathrm{Org}_{43}}{\mathrm{Org}} \quad \text{and} \quad f_{44} = \frac{\mathrm{Org}_{44}}{\mathrm{Org}}, \tag{14}$$

where Org_{43} and Org_{44} are the organic signals at $m/z = 43$ and 44, respectively, and Org is the total organic signal. Lower f_{44} and higher f_{43} are associated with less oxidised, semi-volatile OOA, whereas higher f_{44} and lower f_{43} are associated with more oxidised, low-volatility OOA. Movement towards the upper-left part of an f_{44} versus f_{43} diagram therefore indicates increasing oxygenation and photochemical aging (Ng et al., 2010; Lambe et al., 2011).

4.4.2 Aerosol mass spectrometer measurements

Figure 10 compares several FLOTUS experiments with the ambient-aerosol region measured by Ng et al. (2010) and with the extended flow-reactor region of Lambe et al. (2011). The experiments were conducted at a FLOTUS temperature of 28 °C and a total flow of approximately $17\,\mathrm{L\,min^{-1}}$, with the gate valve to CLOUD closed and the AMS connected to the pickoff pipe. In this figure, the triangles show AP-only experiments, diamonds show IP-only experiments, and crosses show IP with sulfuric acid (SA) generated from photo-oxidation of SO_2. Marker colours indicate the number of illuminated lamps; white markers show dark experiments.

We include one representative dark ozonolysis AP experiment, which lies near the centre of the ambient triangle. Its position is consistent with an intermediate degree of oxidation relative to ambient OOA (Ng et al., 2010). With one lamp illuminated and otherwise unchanged conditions, the AP aerosol shifts towards higher f_{43}, while f_{44} remains low (white triangle towards lowest dark blue triangle in Fig. 10). This initial rightward shift is consistent with the formation and partitioning of relatively less oxidised, carbonyl-containing products during the early stages of photochemical processing (Lambe et al., 2011; Chhabra

https://doi.org/10.5194/egusphere-2026-6281
Preprint. Discussion started: 4 November 2026
© Author(s) 2026. CC BY 4.0 License.

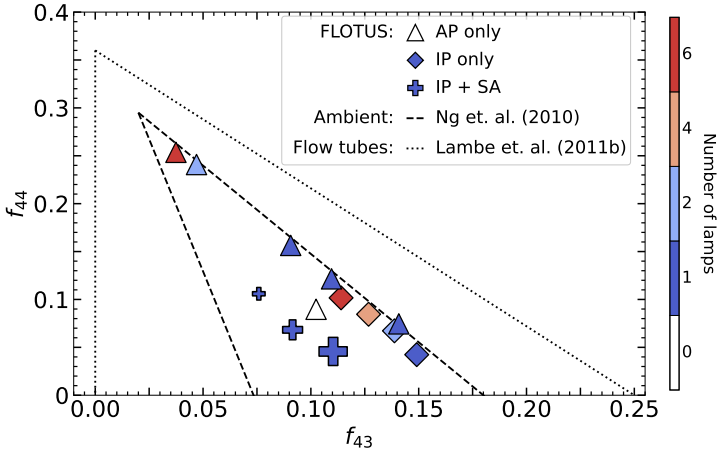


Figure 10. Organic aerosol produced in FLOTUS in f_{44}–f_{43} space measured with an AMS. Triangles show AP-only experiments, diamonds show IP-only experiments, and crosses show IP with sulfuric acid (SA) generated from SO_2. The marker colour illustrates the number of illuminated lamps; the white marker depicts a representative dark experiment with oxidised organics from α-pinene ozonolysis. For the IP+SA subset, smaller crosses represent lower initial IP mixing ratios. The dashed boundary shows the ambient oxygenated organic aerosol (OOA) region (Ng et al., 2010) and the dotted boundary shows the larger laboratory flow-reactor region (Lambe et al., 2011). The experimental conditions were 538–2740 ppbv O_3, 0–2 ppbv AP, 0–12 ppbv SO_2, 29 °C temperature and 4.5 °C dewpoint.

et al., 2011). Increasing O_3 while keeping all other conditions the same then shifts the points toward higher f_{44} and lower f_{43} (following the three dark blue triangles diagonally upwards). This upper-left shift is consistent with increased oxidant exposure and continued oxidation and functionalisation of the AP-derived vapours and products, leading to a greater relative contribution from more oxygenated and organic-acid-containing compounds (Ng et al., 2010; Lambe et al., 2011; Chhabra et al., 2011). At otherwise identical conditions, increasing the number of illuminated lamps, shown by the light blue-towards-red triangles, produces a further shift in the same upper-left direction, consistent with enhanced photochemical oxidant exposure and aging (Ng et al., 2010; Lambe et al., 2011). The resulting rightward-then-upper-left trajectory is consistent with sequential processing of AP SOA, from early-generation oxidation products towards later-generation products with greater oxygenation and acidic functionality (Lambe et al., 2011; Chhabra et al., 2011).

The IP-only experiments, shown as diamonds in Fig. 10, lie at lower f_{44} and higher f_{43} than the AP experiments. This position is consistent with a lower degree of oxidation and a larger relative contribution from less oxidised, non-acid oxygenates (Ng et al., 2010; Lambe et al., 2011; Chhabra et al., 2011). The diagonal sequence of dark-blue, light-blue, orange, and red diamonds represents the same IP concentration and otherwise identical conditions, with an increasing number of illuminated lamps. The progressive movement of these points towards higher f_{44} and lower f_{43} therefore reflects increasing photochemical oxidant exposure and continued oxidation and aging of the IP-derived vapours (Ng et al., 2010; Lambe et al., 2011; Chhabra et al., 2011). This movement is consistent with the formation of later-generation, more oxygenated products and increasing organic acid content during isoprene photooxidation (Lambe et al., 2011; Chhabra et al., 2011).

https://doi.org/10.5194/egusphere-2026-6281
Preprint. Discussion started: 4 November 2026
© Author(s) 2026. CC BY 4.0 License.

The blue crosses in Fig. 10 represent the IP+SO_2 experiments. Adding SO_2 to the IP system produces sulfuric acid seed particles that can take up IEPOX and form IEPOX-derived SOA (D'Ambro et al., 2019). The acidic particle phase therefore introduces an additional acid-mediated uptake and particle-phase processing pathway into the evolution of IP SOA (D'Ambro et al., 2019). The size of the crosses represents the IP concentration, with smaller crosses corresponding to lower IP concentrations. Within the one-lamp IP+SA subset, as the IP concentration decreases the particle composition shifts towards lower f_{43} and higher f_{44}, as shown by the smaller blue crosses moving upwards and to the left in Fig. 10. Decreasing the IP concentration lowers the VOC/oxidant ratio and increases the oxidant availability per IP molecule, favouring successive oxidation steps and the formation of later-generation, more oxygenated and acid-containing products (Lambe et al., 2011; Chhabra et al., 2011). The upper-left displacement of the smaller crosses is therefore consistent with more extensive photochemical processing and aging of the IP-derived oxidation products (Ng et al., 2010; Lambe et al., 2011; Chhabra et al., 2011).

All FLOTUS measurements shown in Fig. 10 lie within the ambient OOA triangle and do not extend into the wider region reported for other laboratory flow-reactor SOA (Ng et al., 2010; Lambe et al., 2011). The measurements demonstrate that FLOTUS can supply organic aerosol with systematically different mass-spectral compositions while reproducing the chemical signatures of OOA observed in the atmosphere (Ng et al., 2010). By controlling the extent of oxidation in FLOTUS, organic vapours and the resulting SOA can be generated at different stages of chemical ageing. These differences in chemical ageing are accompanied by changes in particle properties including volatility, viscosity, and hygroscopicity (Ng et al., 2010, 2011; Lambe et al., 2011; D'Ambro et al., 2019). These differently-aged particles can then be introduced into the CLOUD chamber for detailed studies of their properties and evolution under controlled atmospheric conditions.

5 Summary

We have described here the design and performance of the new FLOw TUbe System, FLOTUS, for the CERN CLOUD chamber. All the experimental conditions of FLOTUS, such as air flow rate, trace gases, relative humidity and temperature, can be controlled independently of CLOUD. The 60 L quartz flow tube is mounted vertically to minimise turbulence from heating by six UV lamps that provide an illumination of up to 114 W optical power at 254 nm. The UV lamps drive intense production of hydroxyl radicals by photolysis of ozone, with measured OH concentrations of up to $3 \cdot 10^9$ cm^{-3} and OH exposures up to $3 \cdot 10^{11}$ $\mathrm{cm}^{-3}\mathrm{s}$.

A static mixer at the narrow-angle conical entrance of the quartz flow tube ensures that trace gases are thoroughly mixed in the air stream and helps prevent the development of recirculation zones in the flow. Our CFD simulations show that the flow develops through the reactor without any resolved eddies up to 50 $\mathrm{L\,min}^{-1}$ flow rate. The measured residence-time distributions of trace toluene pulses confirm that transport is dominated by bulk flow rather than diffusion or turbulence. After the rotational influence of the static mixer has dissipated, the flow is well-characterised by a plug-flow model, which progresses towards a fully-developed laminar flow profile.

The vapours and particles from FLOTUS can either be analysed directly from a pickoff pipe or else transferred to the CERN CLOUD chamber for extended studies with its full suite of state-of-the-art analysing instruments—or a combination of both.

https://doi.org/10.5194/egusphere-2026-6281
Preprint. Discussion started: 4 November 2026
© Author(s) 2026. CC BY 4.0 License.

For all flow configurations, 50 nm particles are efficiently transported along either pipe despite their bends and considerable lengths (3.4 m transfer pipe and 2.7 m pickoff pipe). The transfer efficiencies are lower for sticky vapours of 1 nm mobility size. However, provided the flows are adjusted with additional sheath air to reach the laminar flow limit for each pipe, high transmission efficiencies are achieved of 32 % for transfer to CLOUD and 12 % for the pickoff.

Aerosol particles can be produced in FLOTUS from diverse inorganic and organic precursors, with self-preserving log normal size distributions characteristic of coagulation-dominated growth in the reactor. Aerosol particles are generated with geometric mean diameters between 8.0 and 136 nm, geometric standard deviations between 1.16 and 1.43, and at high rates of up to 10^9 s^{-1}. Measurements of the organic aerosol composition with an Aerosol Mass Spectrometer (AMS) reveal close agreement with ambient aged organic aerosol particles.

In summary, FLOTUS provides precise control of aerosol particle composition and size, and of organic aerosol composition and aging by oxidants. If FLOTUS is operated under warm and humid conditions relative to CLOUD, the generated CCN activate into droplets or ice particles when transferred into the chamber. The initial results reported here therefore establish FLOTUS as an important extension of the CERN CLOUD chamber for novel experiments involving aged organic vapours, cloud condensation nuclei and aerosol-cloud processing.

. Data Availability

All data of all figures is available on the Zenodo database under 10.5281/zenodo.23034226

. Author contributions

E.S., E.U., R.C.F., A.O., S.M. and J.K. designed FLOTUS. M.B. and L-P.D.M. designed and installed the gas system. T.A. designed the thermal control system. E.S., M.B., P.R., I.K., R.K., D.L., L-P.D.M., G.M., S.R., A.O., S.M. and J.K. installed the flow tube and UV system. M.B., Y.H. and S.W. conducted the flow and transport simulations. E.S., M.B., P.R., H.K., N.B., B.M., J.A., M.K.S., P.T., L.H. and J.K. conducted the characterisation experiments. E.S., P.R., H.K., N.B., Z.Z. and J.K. analysed the data. E.S. and M.B. prepared the figures. E.S. and J.K. wrote the manuscript. P.R., H.K., N.B., J.D.V., W.S., P.T., H.H., L.H., P.M.W. and R.C.F provided comments on the manuscript. E.S., M.B., P.R., H.K., N.B., Y.H., B.M., Z.Z., J.A., L.D., J.D.V., M.K.S., P.K., F.K., W.S., P.T., J.V., T.C., J.C., N.D., I.E.H., R.G., A.H., H.H., X-C.H., L.H., H.J., M.K., K.L., O.M., M.P., R.V., P.M.W., R.C.F., A.O., S.M. and J.K. contributed to the scientific discussion. T.C., J.C., N.D., I.E.H., A.H., H.H., X-C.H., H.J., M.K., K.L., O.M., M.P., R.V., P.M.W., R.C.F., A.O. and J.K. acquired funding.

. Competing interests

At least one of the (co-)authors is a member of the editorial board of Atmospheric Measurement Techniques.

https://doi.org/10.5194/egusphere-2026-6281
Preprint. Discussion started: 4 November 2026
© Author(s) 2026. CC BY 4.0 License.



. Acknowledgements

We would like to thank CERN for supporting CLOUD with important technical and financial resources, and for providing a particle beam from the CERN Proton Synchrotron. This work has been supported by European Union's MSCA Doctoral Network CLOUD-DOC 101073026, the Estonian Research Council (projects PRG714, RVTT3, TARISTU24-TK10), the European Union's Horizon 2020 research and innovation programme under grant agreement no. 856612 (EMME-CARE) and the Cyprus Government, the ACCC Flagship funded by the Academy of Finland (grant numbers 337549, 357902, 359340, 374287), the US National Science Foundation (awards AGS-2528506, AGS-2528505 and AGS-2215522), the Swiss national science foundation (project number 200021-213071 and 216181), the German Federal Ministry of Research, Technology and Space (project CLOUD-22 01LK2201A , 01LK2201B and 01LK2201C), the Max Planck Society (MPG) and the Research Council of Finland (grant no. 371185).

https://doi.org/10.5194/egusphere-2026-6281
Preprint. Discussion started: 4 November 2026
© Author(s) 2026. CC BY 4.0 License.

References

ANSYS, Inc.: Ansys Fluent Theory Guide, Canonsburg, Pennsylvania, USA, release 2024 r2 edn., 2024.

Canaval, E., Hyttinen, N., Schmidbauer, B., Fischer, L., and Hansel, A.: NH_4^+ association and proton transfer reactions with a series of organic molecules, Frontiers in Chemistry, 7, 191, 2019.

Chhabra, P., Ng, N., Canagaratna, M., Corrigan, A., Russell, L., Worsnop, D., Flagan, R., and Seinfeld, J.: Elemental composition and oxidation of chamber organic aerosol, Atmospheric Chemistry and Physics, 11, 8827–8845, 2011.

COMSOL AB: COMSOL Multiphysics, version 6.0, COMSOL AB, Stockholm, Sweden, 2021.

D'Ambro, E. L., Schobesberger, S., Gaston, C. J., Lopez-Hilfiker, F. D., Lee, B. H., Liu, J., Zelenyuk, A., Bell, D., Cappa, C. D., Helgestad, T., et al.: Chamber-based insights into the factors controlling epoxydiol (IEPOX) secondary organic aerosol (SOA) yield, composition, and volatility, Atmospheric chemistry and physics, 19, 11 253–11 265, 2019.

Danckwerts, P. V.: Continuous flow systems. Distribution of residence times, Chemical engineering science, 50, 3857–3866, 1995.

Drewnick, F., Hings, S. S., DeCarlo, P., Jayne, J. T., Gonin, M., Fuhrer, K., Weimer, S., Jimenez, J. L., Demerjian, K. L., Borrmann, S., et al.: A new time-of-flight aerosol mass spectrometer (TOF-AMS)—Instrument description and first field deployment, Aerosol science and technology, 39, 637–658, 2005.

Gordon, H., Kirkby, J., Baltensperger, U., Bianchi, F., Breitenlechner, M., Curtius, J., Dias, A., Dommen, J., Donahue, N. M., Dunne, E. M., Duplissy, J., Ehrhart, S., Flagan, R. C., Frege, C., Fuchs, C., Hansel, A., Hoyle, C. R., Kulmala, M., Kürten, A., Lehtipalo, K., Makhmutov, V., Molteni, U., Rissanen, M. P., Stozkhov, Y., Tröstl, J., Tsagkogeorgas, G., Wagner, R., Williamson, C., Wimmer, D., Winkler, P. M., Yan, C., and Carslaw, K. S.: Causes and importance of new particle formation in the present-day and preindustrial atmospheres, Journal of Geophysical Research: Atmospheres, 122, 8739–8760, 2017.

Graus, M., Müller, M., and Hansel, A.: High resolution PTR-TOF: quantification and formula confirmation of VOC in real time, Journal of the American Society for Mass Spectrometry, 21, 1037–1044, 2011.

Hodshire, A. L., Campuzano-Jost, P., Kodros, J. K., Croft, B., Nault, B. A., Schroder, J. C., Jimenez, J. L., and Pierce, J. R.: The potential role of methanesulfonic acid (MSA) in aerosol formation and growth and the associated radiative forcings, Atmospheric Chemistry and Physics, 19, 3137–3160, 2019.

Huang, Y. and Seinfeld, J. H.: A note on flow behavior in axially-dispersed plug flow reactors with step input of tracer, Atmospheric Environment: X, 1, 100 006, 2019.

Huang, Y., Coggon, M. M., Zhao, R., Lignell, H., Bauer, M. U., Flagan, R. C., and Seinfeld, J. H.: The Caltech Photooxidation Flow Tube reactor: design, fluid dynamics and characterization, Atmospheric Measurement Techniques, 10, 839–867, https://doi.org/10.5194/amt-10-839-2017, 2017.

Jayne, J. T., Leard, D. C., Zhang, X., Davidovits, P., Smith, K. A., Kolb, C. E., and Worsnop, D. R.: Development of an aerosol mass spectrometer for size and composition analysis of submicron particles, Aerosol Science & Technology, 33, 49–70, 2000.

Jimenez, J. L., Canagaratna, M., Donahue, N., Prevot, A., Zhang, Q., Kroll, J. H., DeCarlo, P. F., Allan, J. D., Coe, H., Ng, N., et al.: Evolution of organic aerosols in the atmosphere, science, 326, 1525–1529, 2009.

Kang, E., Root, M., Toohey, D., and Brune, W.: Introducing the concept of potential aerosol mass (PAM), Atmospheric Chemistry and Physics, 7, 5727–5744, 2007.

Kirkby, J., Curtius, J., Almeida, J., Dunne, E., Duplissy, J., Ehrhart, S., Franchin, A., Gagné, S., Ickes, L., Kürten, A., Kupc, A., Metzger, A., Riccobono, F., Rondo, L., Schobesberger, S., Tsagkogeorgas, G., Wimmer, D., Amorim, A., Bianchi, F., Breitenlechner, M., David,

https://doi.org/10.5194/egusphere-2026-6281
Preprint. Discussion started: 4 November 2026
© Author(s) 2026. CC BY 4.0 License.

A., Dommen, J., Downard, A., Ehn, M., Flagan, R. C., Haider, S., Hansel, A., Hauser, D., Jud, W., Junninen, H., Kreissl, F., Kvashin, A., Laaksonen, A., Lehtipalo, K., Lima, J., Lovejoy, E. R., Makhmutov, V., Mathot, S., Mikkilä, J., Minginette, P., Mogo, S., Nieminen, T., Onnela, A., Pereira, P., Petäjä, T., Schnitzhofer, R., Seinfeld, J. H., Sipilä, M., Stozhkov, Y., Stratmann, F., Tomé, A., Vanhanen, J., Viisanen, Y., Vrtala, A., Wagner, P. E., Walther, H., Weingartner, E., Wex, H., Winkler, P. M., Carslaw, K. S., Worsnop, D. R., Baltensperger, U., and Kulmala, M.: Role of sulphuric acid, ammonia and galactic cosmic rays in atmospheric aerosol nucleation, Nature, 476, 429–433, 2011.

Kulmala, M., Kontkanen, J., Junninen, H., Lehtipalo, K., Manninen, H. E., Nieminen, T., Petäjä, T., Sipilä, M., Schobesberger, S., Rantala, P., Franchin, A., Jokinen, T., Järvinen, E., äijälä, M., Kangasluoma, J., Hakala, J., Aalto, P. P., Paasonen, P., Mikkilä, J., Vanhanen, J., Aalto, J., Hakola, H., Makkonen, U., Ruuskanen, T., Mauldin, R. L., Duplissy, J., Vehkamäki, H., Bäck, J., Kortelainen, A., Riipinen, I., Kurtén, T., Johnston, M. V., Smith, J. N., Ehn, M., Mentel, T. F., Lehtinen, K. E. J., Laaksonen, A., Kerminen, V.-M., and Worsnop, D. R.: Direct observations of atmospheric aerosol nucleation, Science, 339, 943–946, 2013.

Lambe, A., Onasch, T., Massoli, P., Croasdale, D., Wright, J., Ahern, A., Williams, L., Worsnop, D., Brune, W., and Davidovits, P.: Laboratory studies of the chemical composition and cloud condensation nuclei (CCN) activity of secondary organic aerosol (SOA) and oxidized primary organic aerosol (OPOA), Atmospheric Chemistry and Physics, 11, 8913–8928, 2011.

Lee, K.: Change of particle size distribution during Brownian coagulation, Journal of Colloid and Interface Science, 92(2), 315–325, 1983.

Lee, K., Lee, Y., and Han, D.: The log-normal size distribution theory for Brownian coagulation in the low Knudsen number regime, Journal of Colloid and Interface Science, 188(2), 486–492, 1997.

Leonard, B. P.: A stable and accurate convective modelling procedure based on quadratic upstream interpolation, Computer methods in applied mechanics and engineering, 19, 59–98, 1979.

Levenspiel, O.: Chemical reaction engineering, Industrial & engineering chemistry research, 38, 4140–4143, 1999.

Mellouki, A., Ammann, M., Cox, R. A., Crowley, J. N., Herrmann, H., Jenkin, M. E., McNeill, V. F., Troe, J., and Wallington, T. J.: Evaluated kinetic and photochemical data for atmospheric chemistry: volume VIII–gas-phase reactions of organic species with four, or more, carbon atoms ($\geq$ C 4), Atmospheric Chemistry and Physics, 21, 4797–4808, 2021.

Menter, F. R.: Two-equation eddy-viscosity turbulence models for engineering applications, AIAA journal, 32, 1598–1605, 1994.

Miljevic, B., Mallet, M., Osuagwu, C. G., Ristovski, Z., Humphries, R. S., Selleck, P., Taylor, S., and Keywood, M.: Aerosol acidity controls methanesulfonic acid evaporation from aerosols during Antarctic katabatic outflow, Communications Earth & Environment, 6, 1057, 2025.

Ng, N., Canagaratna, M., Zhang, Q., Jimenez, J., Tian, J., Ulbrich, I., Kroll, J., Docherty, K., Chhabra, P., Bahreini, R., et al.: Organic aerosol components observed in Northern Hemispheric datasets from Aerosol Mass Spectrometry, Atmospheric Chemistry and Physics, 10, 4625–4641, 2010.

Ng, N., Canagaratna, M., Jimenez, J., Chhabra, P., Seinfeld, J., and Worsnop, D.: Changes in organic aerosol composition with aging inferred from aerosol mass spectra, Atmospheric Chemistry and Physics, 11, 6465–6474, 2011.

Patankar, S. V. and Spalding, D. B.: A calculation procedure for heat, mass and momentum transfer in three-dimensional parabolic flows, in: Numerical prediction of flow, heat transfer, turbulence and combustion, pp. 54–73, Elsevier, 1983.

Peng, Z., Day, D., Stark, H., Li, R., Lee-Taylor, J., Palm, B., Brune, W., and Jimenez, J.: HO x radical chemistry in oxidation flow reactors with low-pressure mercury lamps systematically examined by modeling, Atmospheric Measurement Techniques, 8, 4863–4890, 2015.

Seinfeld, J. H. and Pandis, S. N.: Atmospheric Chemistry and Physics: From Air Pollution to Climate Change, Wiley, Hoboken, New Jersey, 3rd edn., 2016.

https://doi.org/10.5194/egusphere-2026-6281
Preprint. Discussion started: 4 November 2026
© Author(s) 2026. CC BY 4.0 License.



Taylor, G.: Dispersion of soluble matter in solvent flowing slowly through a tube, Proceedings of the Royal Society of London. Series A, Mathematical and Physical Sciences, pp. 186–203, 1953.

Wang, S. C. and Flagan, R. C.: Scanning electrical mobility spectrometer, Aerosol Science and Technology, 13, 230–240, 1990.

595 Zhao, Z., Crittenden, J. C., Zhao, H., and Chen, Y.: The self-preserving size distribution of fractal aggregates coagulating by Brownian motion and simultaneous fluid shear at low Peclet numbers: numerical solutions, Journal of Aerosol Science, 87, 1–16, 2015.